

The parallax zero point offset from *Gaia* EDR3 data [★]

M. A. T. Groenewegen

Koninklijke Sterrenwacht van België, Ringlaan 3, B-1180 Brussels, Belgium
e-mail: martin.groenewegen@oma.be

received: ** 2021, accepted: * 2021

ABSTRACT

The second data release of *Gaia* revealed a parallax zero point offset of -0.029 mas based on quasars. The value depended on the position on the sky, and also likely on magnitude and colour. The offset and its dependence on other parameters inhibited an improvement in the local distance scale using e.g. the Cepheid and RR Lyrae period-luminosity relations. Analysis of the recent *Gaia* Early Data Release 3 (EDR3) reveals a mean parallax zero point offset of -0.021 mas based on quasars. The *Gaia* team addresses the parallax zero point offset in detail and proposes a recipe to correct for it, based on ecliptic latitude, *G*-band magnitude, and colour information. This paper is a completely independent investigation into this issue focussing on the spatial dependence of the correction based on quasars and the magnitude dependence based on wide binaries. The spatial and magnitude corrections are connected to each other in the overlap region between $17 < G < 19$. The spatial correction is presented at several spatial resolutions based on the HEALPix formalism. The colour dependence of the parallax offset is unclear and in any case secondary to the spatial and magnitude dependence. The spatial and magnitude corrections are applied to two samples of brighter sources, namely a sample of ~ 100 stars with independent trigonometric parallax measurements from *HST* data, and a sample of 75 classical cepheids using photometric parallaxes. The mean offset between the observed GEDR3 parallax and the independent trigonometric parallax (excluding outliers) is about $-39 \mu\text{as}$, and after applying the correction it is consistent with being zero. For the classical cepheid sample it is suggested that the photometric parallaxes may be underestimated by about 5%.

Key words. Stars: distances - parallaxes

1. Introduction

Data from the *Gaia* mission (Gaia Collaboration et al. 2016) has impacted most areas in astronomy. One the fields were the *Gaia* 2nd data release (GDR2, Gaia Collaboration et al. 2018) was eagerly awaited was in reliably establishing the local distance scale through calibration of the period-luminosity (*PL*) relation of classical cepheids (CCs) and RR Lyrae (RRL) variables.

Riess et al. (2018b) analysed a sample of 50 CCs. They derived a parallax zero point offset (hereafter PZPO) of -0.046 ± 0.013 mas, compared to the -0.029 mas derived for quasars by Lindegren et al. (2018) and concluded that the need to independently determine the PZPO largely countered the higher accuracy of the parallaxes in determining an improved zero point of the *PL*-relation. Independently, Groenewegen (2018) (hereafter G18) derived a PZPO of -0.049 ± 0.018 mas based on a comparison of nine CCs with the best non-*Gaia* parallaxes (mostly from *HST* data). Ripepi et al. (2019) re-classified all 2116 stars reported by Clementini et al. (2019) to be Cepheids in the Milky Way (MW). Period-Wesenheit relations in the *Gaia* bands were presented. Assuming a canonical distance modulus to the LMC of 18.50, a *Gaia* PZPO of ~ -0.07 to -0.1 mas was found. PZPOs based on GDR2 data were also reported for RRL stars (~ -0.056 mas, Muraveva et al. 2018; -0.042 ± 0.013 mas, Layden et al. 2019), and many other classes of objects (Stassun & Torres 2018, Graczyk et al. 2019, Xu et al. 2019, Schönrich et al. 2019). These values were mostly all-sky

averages, but when sufficient data was available it was clear that the PZPO depended on position in the sky, magnitude, and colour (Zinn et al. 2019; Khan et al. 2019; Leung & Bovy 2019; Chan & Bovy 2020).

The *Gaia* Early Data Release 3 (GEDR3) presents the most recent information on parallax, proper motions, position and colour information for about 1.8 billion objects (Gaia Collaboration et al. 2021a). Lindegren et al. (2021b) presents the general properties of the astrometric solution, while Lindegren et al. (2021a) (hereafter L20) specifically addresses the PZPO and make a python script available to the community in order to calculate the PZPO. This module gives PZPO (without an error bar) as a function of input parameters ecliptic latitude (β), *G*-band magnitude, the `astrometric_params_solved` parameter (Lindegren et al. 2021b), and either the effective wavenumber of the source used in the astrometric solution (ν_{eff} , `nu_eff_used_in_astrometry` for the 5-parameter solution `astrometric_params_solved=31`) or the astrometrically estimated pseudo colour of the source (`pseudocolour`) for the 6-parameter solution (`astrometric_params_solved=95`). The module is defined in the range $6 < G < 21$ mag, $1.72 > \nu_{\text{eff}} > 1.24 \mu\text{m}^{-1}$, corresponding to about $0.15 < (G_{\text{BP}} - G_{\text{RP}}) < 3.0$ mag where *G*, *G_{BP}*, and *G_{RP}* are the magnitudes in the *Gaia* G-, Bp-, and Rp-band, respectively.

Several papers have already applied the L20 correction to the raw GEDR3 parallaxes. Riess et al. (2021) applied it to a sample of 75 CCs in the Milky Way ($6.1 \lesssim G \lesssim 11.2$ mag, $0.9 \lesssim (G_{\text{BP}} - G_{\text{RP}}) \lesssim 2.5$ mag). For this sample, there is a strong dependence of the correction on β (ranging from -4 to $-38 \mu\text{as}$) with only a small dependence (of order $1.8 \mu\text{as}$) on magnitude and colour,

Send offprint requests to: Martin Groenewegen

* Table 1 is available in electronic form at the CDS via anonymous ftp to cdsarc.u-strasbg.fr (130.79.128.5) or via <http://cdsweb.u-strasbg.fr/cgi-bin/qcat?J/A+A/>.

with a median correction of $-24 \mu\text{as}$. Allowing for a remaining PZPO after application of the L20 correction and fitting the data to the independently calibrated PL relation of CCs in the Large Magellanic Cloud (LMC) reveals an offset of $14 \pm 6 \mu\text{as}$, in the sense that the L20 corrections are too much negative, that is the values are over corrected.

A similar conclusion is reached by Zinn (2021) who analysed a sample of 2000 first-ascent red-giant branch stars with asteroseismic parallaxes in the *Kepler* field ($9.0 \lesssim G \lesssim 13.0$ mag, $1.0 \lesssim (G_{\text{BP}} - G_{\text{RP}}) \lesssim 2.3$ mag) and concludes that the L20 corrections are too much negative by $15 \pm 3 \mu\text{as}$ for $G \lesssim 10.8$ mag.

Bhardwaj et al. (2021) apply a theoretical period-luminosity-metallicity relation in the *K*-band to a sample of about 350 Milky Way RR Lyrae stars ($8.9 \lesssim G \lesssim 17.8$ mag, $0.4 \lesssim (G_{\text{BP}} - G_{\text{RP}}) \lesssim 1.3$ mag) to find a ZP of $(-7 \pm 3) \mu\text{as}$ when compared to the raw GEDR3 parallaxes. The mode of the L20 correction for this sample is $-32 \pm 4 \mu\text{as}$ so, again, the L20 formula over corrects the parallaxes, in this case by $25 \pm 5 \mu\text{as}$.

Stassun & Torres (2021) continue their previous analysis using eclipsing binaries as reference objects. Stassun & Torres (2018) found an offset of $(-82 \pm 33) \mu\text{as}$ based on 89 stars from GDR2 while, while their latest analysis using GEDR3 indicates an offset of $(-37 \pm 20) \mu\text{as}$ based on 76 objects ($5 \lesssim G \lesssim 12$ mag, $-0.1 \lesssim (G_{\text{BP}} - G_{\text{RP}}) \lesssim 2.2$ mag). After applying the L20 correction the PZPO becomes $(-15 \pm 18) \mu\text{as}$, indicating no over- or under-correction.

Huang et al. (2021) use a sample of over 69 000 primary red clump (PRC; $9.5 \lesssim G \lesssim 15$ mag, $1.32 \lesssim \nu_{\text{eff}} \lesssim 1.5$, or about $1.0 \lesssim (G_{\text{BP}} - G_{\text{RP}}) \lesssim 2.2$ mag) stars based on LAMOST data from Huang et al. (2020). The distances come from Schönrich et al. (2019) that are based on a Bayesian analysis of DR2 data and include an PZPO of -0.054 mas. The reference distance is compared to the raw GEDR3 parallax, and the GEDR3 parallax after applying the L20 correction. The difference (*Gaia* - PRC) is -26 in the former and $+3.7 \mu\text{as}$ in the latter case (no errors are reported). They also show the trends of the parallax difference against G , ν_{eff} , and ecliptic latitude. They show that applying the L20 correction removes some of these trends (in particular against G magnitude), but not all, and show that there is a trend with ecliptic longitude, especially for ecliptic latitudes $< 30^\circ$.

The aim of the present paper is to have an independent (and alternative) investigation into the PZPO, and in particular into the spatial dependence. This will be achieved by using a large sample of reliable QSOs (selected differently from the sample used in various GEDR3 papers). In addition physical binaries will be considered to derive the dependence of the PZPO on G magnitude. At the bright end the PZPO derived in the present paper will be applied to a sample of stars that has not been systematically considered in previous works, namely stars that have an independent parallax measurement from the *Hubble Space Telescope* (HST). In addition, the PZPO will be applied to the sample of CCs by Riess et al. (2021), and results will be compared to using the correction in L20.

The paper is structured as follows. In Section 2 the main methodology is introduced. In Section 3 the sample of stars is described. Section 4 presents the results of the calculations and the derivation of the PZPO, while Sect. 5 applies the PZPO to the QSO sample itself and the two samples of stars. A brief discussion and summary concludes the paper.

2. Methodology

The parallax zero point offset is defined through

$$\pi_t = \pi_o - \text{ZP} \quad (1)$$

where π_t is the true parallax and π_o the observed parallax (as listed in the GEDR3 catalogue). The PZPO is parameterised in the present paper as a sum of linear functions that are assumed to hold over a range in magnitudes:

$$\begin{aligned} \text{ZP} &= C_0(\alpha, \delta) + C_1 (G - \text{Gref}) + C_2 (G - \text{Gref})^2 \\ &\quad + C_3 ((G_{\text{BP}} - G_{\text{RP}}) - \text{BRref}) \end{aligned} \quad (2)$$

$$= \pi_o - \pi_t$$

where Gref= 20.0 mag and BRref= 0.8 mag are reference values. They are chosen to represent the typical colours of QSOs.

In the present analysis also binaries are considered. In that case the true parallaxes for the two components are essentially the same and as they are essentially at the same position on the sky the C_0 term may be assumed to cancel out. The difference of Eq. 2 for the two components (labelled as subscripts as primary, p, and secondary, s) becomes:

$$\begin{aligned} \Delta \text{ZP} &= C_1 (G_p - G_s) + \\ &\quad C_2 ((G_p - \text{Gref})^2 - (G_s - \text{Gref})^2) + \\ &\quad C_3 ((G_{\text{BP}} - G_{\text{RP}})_p - (G_{\text{BP}} - G_{\text{RP}})_s) + \epsilon \end{aligned} \quad (3)$$

$$= (\pi_o)_p - (\pi_o)_s$$

where ϵ is a term that can be thought off as the spatial correlation on the extent of the binary separation.

The difference between the formalism outlined in Appendix A in L20 and that is used here is two-fold. The main difference is that the spatial dependence is made explicit here rather than using a second-order polynomial in $\sin \beta$. The other difference is that the spatial, magnitude and colour dependence are assumed to be separable while the L20 correction allows for cross-terms.

The term C_0 is allowed to vary over the sky and the HEALPix formalism (Górski et al. 2005, the NESTED variant) is used to transform (α, δ) to a sky pixel. This is done using a implementation in python, HEALPy (Zonca et al. 2019). The number of sky pixels depends on the chosen resolution; resolution levels 0, 1, 2, 3, and 4 are considered in the present paper which correspond to 12, 48, 192, 768 and 3072 pixels, respectively. The highest resolution corresponds to a mean spacing of 3.7 degrees between sky pixels.

The fitting of Eqs. 2 or 3 to the data is done with the singular value decomposition algorithm (routine *svdfit*) as implemented in Fortran77 in Press et al. (1992). This algorithm minimises the χ^2 taking into account the errors in the ordinate (the parallax (difference)) and gives the best-fit parameter values with error bars. In order to also consider the errors in magnitudes and colours Monte Carlo simulations are performed where new datasets are generated taking into account Gaussian errors in the parallaxes, magnitudes, and colours. The parameter values quoted below (in Table 2) are the median values for the parameters among these simulations with as error the dispersion among the parameter values, calculated as 1.4826 times the median-absolute-deviation (MAD), equivalent to 1σ in a Gaussian distribution.

3. The sample

In order to apply Eq. 2 or 3 and determine ZP as a function of sky position, magnitude and colour a large sample of sources with known true distances is required. In this paper QSOs, physical binaries, and stars with an independent trigonometric parallax determination will be considered.

For the samples discussed below the following parameters were retrieved from the GEDR3 main catalogue¹: parallax and parallax error (`parallax`, `parallax_error`), proper motion in Ra and Dec with errors (`pmra`, `pmra_error`, `pmdec`, `pmdec_error`), the source identifier (`source_id`)², which parameters have been solved for (`astrometric_params_solved`; five- and six-parameter solutions are relevant for the present paper, see Lindegren et al. 2021b), the renormalised unit weight error (RUWE), the goodness-of-fit (GOF, `astrometric_gof_all`), the effective wavenumber of the source used in the astrometric solution (`νeff`, `nu_eff_used_in_astrometry`), the astrometrically estimated pseudocolour of the source (`pseudocolour`), the G , G_{BP} , and G_{RP} magnitudes with errors (`phot_g_mean_mag`, `phot_g_mean_mag_error`, `phot_bp_mean_mag`, `phot_bp_mean_mag_error`, `phot_rp_mean_mag`, `phot_rp_mean_mag_error`).

3.1. Quasars

Several of the GEDR3-team papers use a QSO sample (Gaia Collaboration et al. 2021b; Lindegren et al. 2021b,a) but the paper describing the selection of this sample has not been published at the time of submission. What is available is the list of 1.61 million `source_ids` which contains a reference to a catalogue but without any quality flag. For this reason, and because this project started before the release of GEDR3, a different QSO sample was created.

The Million Quasars (Milliquas) catalog (version 7.0b, Flesch 2019) is used which contains of order 830 000 type-I QSOs and AGN plus about 500 000 quasar candidates. From the full catalogue the 1.37 million objects with a confirmed redshift > 0.1 or a probability of being a quasar of $> 98\%$ are selected. The cross-match facility (xMatch) at the Centre des Données (CDS) in Strasbourg was used to match this list with GEDR3 using a search radius of $0.15''$, and this returned 998 220 matches, of which 855 518 QSOs have a parallax, G , G_{BP} , and G_{RP} magnitude available. The true parallax for these sources is assumed to be zero.

First the general properties of the QSO sample are discussed in particular the distribution of the GOF and the RUWE. It is recalled that the GOF parameter should follow a Gaussian distribution with zero mean and unit dispersion (Wilson & Hilferty 1931). In GDR2 this was not the case due to the "degree-of-freedom" bug (see Appendix A in Lindegren et al. 2018 and the discussion in Groenewegen 2018). The RUWE was introduced after GDR2 (Lindegren 2018) as an other quality indicator of the astrometric solution. It compared the unit-weight-error (UWE, the square-root of the reduced χ^2) to that of a sample of unproblematic stars as a function of magnitude and colour. Although the χ^2 values were actually numerically incorrect the ratio of the UWEs was probably deemed representative of the relative quality of the astrometric solution. In Gaia EDR3, the "degree-

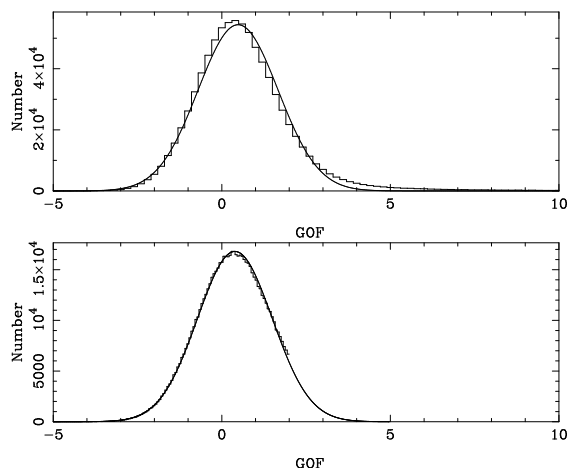


Fig. 1. Distribution of the GOF with a Gaussian fit. Top panel, the about 841 000 QSO with parallaxes and PMs consistent with zero. A significant tail toward large GOF is visible. Lower panel, the fit with GOF restricted to $< +2.0$.

of-freedom" bug has been corrected and the GOF is the main parameter to describe the quality of the astrometric solution.

Although the QSO sample was selected to be pure it still contains non-QSOs. As QSOs should have zero parallax and proper motion (within the error bars) the following conditions are applied:

$$|(\pi + 0.0202)| / \sigma_\pi < 5$$

$$(\text{PMRA} / \sigma_{\text{PMRA}})^2 + (\text{PMDE} / \sigma_{\text{PMDE}})^2 < 25$$

where -0.0202 mas is the average offset of QSOs (see below). Similar cuts were applied to the QSO sample in Lindegren et al. (2021a), but no selection on `astrometric_params_solved` and ν_{eff} is applied. The 5σ limit on the parallax and proper motions (PMs) in Ra and Dec corresponds to the expected level of outliers following Chauvenet's criterion with ~ 800 000 objects.

The upper panel in Figure 1 shows the distribution of the GOF for the 841 000 QSOs that remain after applying the selection on parallax and PM, together with a Gaussian fit. The mean and dispersion are 0.483 and 1.187 with negligible formal errors. The mean is slightly larger than expected but the tail to negative GOF (the extreme value is -5.4) is not inconsistent with the distribution. On the other hand the tail to larger GOF (the extreme value is $+200$) is obvious. To obtain a better estimate of the mean and width of the distribution undisturbed by outliers, the lower panel shows the distribution when the GOF and the Gaussian fit to the distribution is restricted to $< +2.0$. The mean is 0.388 with $\sigma = 1.109$. Based on this analysis a condition $-4 < \text{GOF} < 5$ is imposed on all selections described in this paper, allowing for a small excess of sources towards larger GOF. Figure 2 shows the distribution in G , $(G_{BP} - G_{RP})$ colour, and RUWE after imposing these conditions, as well as $\text{RUWE} < 1.4$ to eliminate a few extreme outliers in that parameter. The distribution in RUWE has a peak slightly above one, consistent with the fact that the distribution in GOF peaks slightly above zero. It indicates that the error bars in the parallax are likely underestimated by a few percent (at least in this range of magnitude and colour), consistent with the findings in Fabricius et al. (2021) and El-Badry et al. (2021). A final sample of 824 819 QSOs is retained. The median parallax in that sample is -0.0202 mas with a dispersion (calculated as 1.4826 times the MAD) of 0.393 mas.

¹ The data is downloaded from the copy available via ViZier at the CDS.

² The `source_id` can also be used to determine the pixel in the HEALPix scheme, as `source_id / (235 · 4(12-level))`.

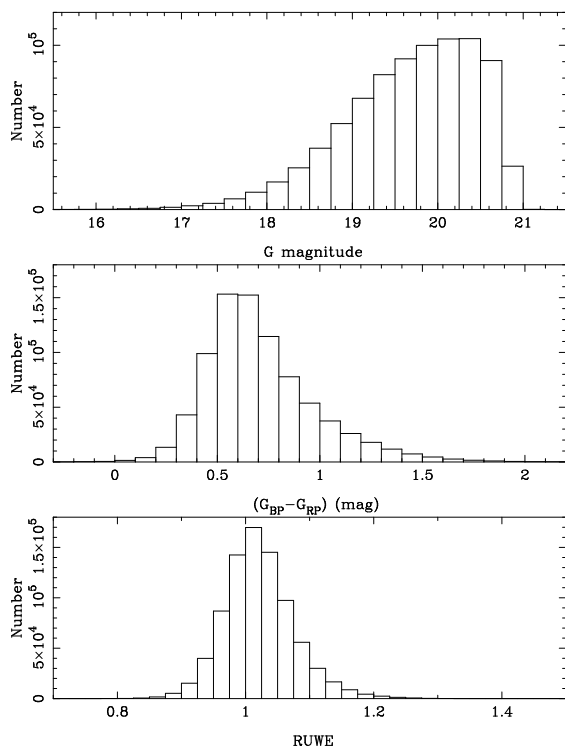


Fig. 2. Distribution of G , $(G_{BP} - G_{RP})$ colour and RUWE for the QSO sample after applying selections on parallax, proper motion, GOF, and RUWE.

3.2. Wide binaries

In this paper the catalogue of wide binaries (WBs) of El-Badry et al. (2021) is used which is based on GEDR3 data. In its raw form it contains 1.8 million candidate physical binaries. For wide and close-by binaries the hypothesis that both components are essentially at the same physical distance may no longer be correct. The procedure outlined in Sect. 5 of that paper is used to eliminate objects where the true parallax difference between the two stars (Eq. 13 of that paper) is estimated to contribute more than 5% to the error in the observed parallax differences (eliminating about 14 000 of the 1.8 million pairs). The sample is also restricted to the subset of about 784 000 pairs with a <1% probability of chance alignment, which is stricter than the high-confidence sample (chance alignment <10%) of 1.2 million objects considered in El-Badry et al. (2021).

Fabricius et al. (2021) and Lindegren et al. (2021a) also consider samples of binaries to validate the GEDR3 results and analyse the PZPO, respectively. Both samples are directly constructed from GEDR3 data (but they are not identical) and careful selection is needed to reach a pure sample.

3.3. Sources with trigonometric parallax determinations

The *Fine Guidance Sensor* (FGS) and the *Wide Field Camera 3* (WFC3) on board the *Hubble Space Telescope* (HST) have been used to determine parallaxes and proper motions. The review of Benedict et al. (2017) describes the methodology and provides a list of 105 targets for which the parallax has been determined by using the FGS. Some close binaries are included in the list with both components. One component was removed from the list as the binary can not be resolved by *Gaia*. Some recent works by van Belle et al. (2020) and Bond et al. (2018) (on Polaris B) are added to give a list of 102 targets. The method-

ology to use the WFC3 to obtain parallaxes was described in Riess et al. (2014) and Casertano et al. (2016) and has been used to obtain distances to eight CCs (Riess et al. 2014, 2018a). Although parallaxes from *Hipparcos* are in general no longer competitive when compared to *Gaia*, Table 1 includes one exception, Polaris A, the most nearby CC, that had no parallax listed in GDR1 and GDR2.

The independent trigonometric parallax data and basic GEDR3 data on the 111 objects are listed in Table 1. Only one object is not listed in GEDR3 (Polaris A), and 8 objects have no parallax listed (all these have exceptionally large GOF values). Applying the selection on GOF and RUWE further eliminates 37 objects for a useful sample of 57 objects.

4. Results

In this section the results are being discussed related to the derivation of the PZPO correction.

4.1. QSOs

Figure 3 gives another representation of the QSO sample, similar to Fig. 5 in L20. It shows a binned version of the PZPO (weighted mean and error) as a function of G magnitude, $(G_{BP} - G_{RP})$ colour (L20 shows it as a function of ν_{eff}), and β . The lines in the top and middle panels are not fits to the data but represent the finally applied corrections based on a full analysis (see later in this section, Eqs. 4, 5). In the middle panel, the line does not seem to fit the points very well. This is related to the fact that in the QSO sample the brighter QSOs are bluer than fainter ones. In addition, the error bar on this slope is quite large.

Although the QSO sample is different from that used in GEDR3-team papers the behaviour is very similar to that shown in L20, as expected. There is a quite noticeable correlation with G for $G \gtrsim 17$ mag, a small (if any) correlation with colour (or ν_{eff}), and a relatively modest correlation with β . In particular the latter correlation is interesting. An identical binning is used as in L20 (40 bins) and the distribution of the black open squares is quasi identical to that shown in L20. The blue points show another representation, and the main reason why a different spatial dependence of the PZPO is proposed here. The binning is now done based on HEALPix level 1, which has 48 pixels, very similar to the binning in L20. The point and the vertical error bar have the same meaning, while the horizontal line represents the range in β for that HEALPix pixel. One can clearly observe a significantly larger spread even for pixels with very similar ecliptic latitudes. This indicates that the PZPO is a more complicated function than of β alone. The result is qualitatively similar to Huang et al. (2021) who demonstrate that there is a trend of the PZPO with ecliptic longitude, especially for $\beta < 30^\circ$.

To investigate this further Eq. 2 is fit to this sample, solving for C_0 (only a spatial component), $C_0 + C_1 + C_2$, and all parameters. This is done for several HEALPix levels, and the results are summarised in Table 2. As the fitting routine is based on minimising the χ^2 one expects the value for C_0 to be equal to the weighted mean of the parallaxes of all QSOs in that pixel when only the spatial component is solved for. As a sanity check to the implementation of the numerical code it was verified that this is indeed the case.

As the distribution of known quasars is not uniform over the sky (typically underrepresented in the Galactic plane) the number of objects per sky pixel varies strongly. At HEALPix level 3 there are 10 pixels with no QSOs, and 63 with 40 or less objects. On the other hand 50% of pixels have 810 objects or more,

with a maximum of 3762. Inspecting the error in the parallax offset and the signal-to-noise suggests that forty objects or more are required for the results to be robust. The median offset over these 706 pixels is $-21.0 \mu\text{as}$ with a dispersion over the pixels (calculated via the MAD) of $12.4 \mu\text{as}$ when fitting only the spatial component. Averaging only over the pixels with 100 objects or more changes the parameter and the error by $\sim 0.3 \mu\text{as}$.

The first entries in Table 2 (models 1-9) include all QSOs but based on the trends seen in Fig. 3 models restricted in G magnitude are more realistic, and several ranges have been explored. Models 10-28 show the main the results, and based on these the following linear correction of the parallax is proposed (in $\mu\text{as}/\text{mag}$) in the range $G > 17 \text{ mag}$ ($\Delta\pi$ to be subtracted from the catalogued GEDR3 parallax):

$$\Delta\pi = \begin{cases} +6.0 (G - 19.9) & 17.0 \leq G < 19.9 \\ +0.0 & 19.9 \leq G < 20.0 \\ -16.0 (G - \text{Gref}) & 20.0 \leq G < 22.5 \end{cases} \quad (4)$$

The presence of a colour dependence is less clear. As can be seen from the results in Table 2 the term is not very significant (at the 2σ level at best). Nevertheless, the colour correction (in $\mu\text{as}/\text{mag}$) that will be tested is:

$$\Delta\pi = -3.5 ((G_{\text{BP}} - G_{\text{RP}}) - \text{BRref}) \quad (5)$$

Figure 3 shows no real trend with magnitude for brighter magnitudes. Fitting a constant at HEALPix level 0, as there are only ~ 3300 QSOs brighter than 17 mag, gives a value of about $-31 \mu\text{as}$ (model 29).

Models 30-34 and 35-39 give the results when the parallaxes are corrected according to Eq. 4, respectively, Eq. 4 and 5. The results are listed for several HEALPix levels. The average spatial correction of the PZPO (at $G = 20$) is essentially independent of the chosen HEALPix level and suggests systematic errors of $\lesssim 0.5 \mu\text{as}$. Tests using a slope of -6.1 , respectively, 17.0 , at the bright and faint magnitude end, and shifting the nodes by 0.1 mag indicate global differences of $\lesssim 0.2 \mu\text{as}$ and changes in the spatial PZPO in individual pixels of $\lesssim 0.2\sigma$. Adding the colour correction increases the dispersion over the pixels, suggesting again that the colour term is not a significant factor.

The detailed results of models 30-39 are available through the CDS, and an example of the content is given in Tab. 3. These files list the PZPO and error for each individual HEALPix pixel for levels 0, 1, 2, 3, and 4, and the number of QSOs in each pixel.

Some properties are summarised in Tab. 4. It lists the HEALPix level, the number of pixels, the number of pixels with only 0 or 1 object, and in column 4 the range in the PZPO errors for the pixels with 40 or more objects, which typically increases with increasing spatial resolution.

Figure 4 illustrates how this spatial and magnitude correction works for the QSO sample with $G > 17 \text{ mag}$. The black open circles give the observed parallaxes of the 821 000 QSOs averaged and binned over $\sin\beta$. The blue open circles give the L20 correction for the individual QSOs again averaged and binned over $\sin\beta$, while the black filled circles give the corrected parallaxes according to Eq. 4 and the red filled circles the spatial correction at HEALPix level 2. Weighted averages are used except for the blue circles of the L20 correction. The unweighted mean is shown as the L20 correction carries no error. The shape of the L20 correction is due to the fact that L20 uses a second order polynomial in $\sin\beta$ (Eq. A4 in L20 and the discussion in their Sect. 4.1). The spatial correction at HEALPix level 2 gives a good description of the parallaxes corrected according to Eq. 4

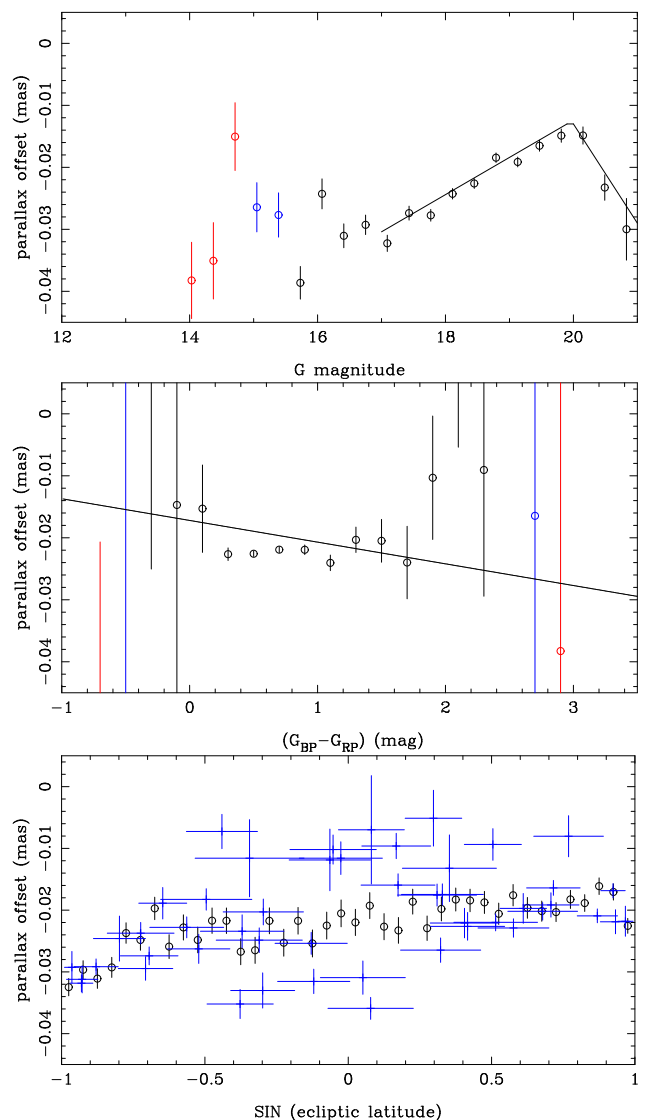


Fig. 3. PZPO for the QSO sample as a function of G , $(G_{\text{BP}} - G_{\text{RP}})$ colour and ecliptic latitude (open circles). Only bins with ≥ 5 objects are plotted. Bins with 100 objects or less are plotted in blue, with 30 objects or less in red. The lines in the top panel and the lines in the middle panel are *not* a fit to the data, but are based on Eq. 4. The blue points in the lower panel indicate the PZPO for the 48 HEALPix level 1 pixels. The horizontal bar gives the range in $\sin\beta$ for each HEALPix pixel.

even though the fitting was done according to the HEALPix level and not specifically to ecliptic latitude. Section 5.1 discusses the results when the correction in L20 and the current one are applied to the QSO sample.

4.2. Wide binaries

The top panel in Fig. 5 shows a binned version of the parallax difference between the primary and secondary component as a function of primary G in the top panel. A similar diagrams was shown in Fabricius et al. (2021) (their Fig. 22) What is striking is the sharp decrease of the parallax difference for faint magnitudes. This is due to selection effects in the El-Badry et al. (2021) sample. Readily visible in the bottom panel are the conditions $\pi_p > 1$ and $\pi_s > 1 \text{ mas}$ that were imposed (but there are others on the (relative) parallax accuracy, see their section 2),

Table 2. Result of the fitting to the QSO sample.

Model	HEALPix level	$\langle C_0 \rangle$ (μas)	N	C_1 ($\mu\text{as}/\text{mag}$)	C_2 ($\mu\text{as}/\text{mag}^2$)	C_3 ($\mu\text{as}/\text{mag}$)
all G magnitudes						
1	2	-20.6 ± 9.0	190/192	-	-	-
2	2	-14.5 ± 9.2	190/192	4.00 ± 0.25	-	-
3	2	-13.8 ± 8.9	190/192	4.91 ± 0.63	0.24 ± 0.13	-
4	2	-14.1 ± 9.0	190/192	5.16 ± 0.60	0.29 ± 0.14	-3.08 ± 1.16
5	3	-21.0 ± 12.4	706/768	-	-	-
6	3	-14.9 ± 12.2	706/768	3.97 ± 0.23	-	-
7	3	-14.2 ± 12.7	706/768	5.07 ± 0.60	0.29 ± 0.13	-
8	3	-14.9 ± 12.5	706/768	5.18 ± 0.65	0.28 ± 0.13	-3.61 ± 1.23
9	4	-15.1 ± 19.0	2600/3072	4.85 ± 0.45	0.22 ± 0.08	-3.96 ± 1.67
$17 < G < 20$						
10	1	-12.1 ± 7.4	48/48	5.97 ± 0.41	-	-
11	2	-20.7 ± 9.0	190/192	-	-	-
12	2	-12.4 ± 9.1	190/192	6.03 ± 0.32	-	-
13	2	-12.5 ± 9.2	190/192	6.11 ± 0.44	-	-3.55 ± 1.49
14	2	-13.4 ± 9.2	190/192	4.13 ± 1.51	-0.71 ± 0.52	-
15	2	-13.2 ± 9.3	190/192	4.54 ± 1.71	-0.53 ± 0.54	-3.17 ± 1.35
16	3	-12.5 ± 12.6	698/768	6.05 ± 0.45	-	-
17	3	-12.9 ± 12.5	698/768	4.70 ± 1.32	-0.53 ± 0.50	-4.06 ± 1.55
$19.875 < G < 20.125$						
18	0	-13.4 ± 6.5	12/12	-	-	-
19	1	-14.3 ± 11.3	47/48	-	-	-
20	2	-12.8 ± 22.0	180/192	-	-	-
21	3	-13.6 ± 44.2	595/768	-	-	-
22	4	-13.5 ± 62.8	921/3072	-	-	-
$20.125 < G < 22.5$						
23	1	-22.5 ± 23.8	47/48	-	-	-
24	1	-16.8 ± 22.1	47/48	-16.35 ± 7.90	-	-
25	2	-13.86 ± 33.3	182/192	-15.64 ± 9.59	-	-
26	2	-13.39 ± 33.1	182/192	-16.30 ± 7.30	-	-3.71 ± 4.17
27	2	-13.99 ± 34.2	182/192	-15.36 ± 30.71	-1.96 ± 33.7	-3.21 ± 5.51
28	3	-15.4 ± 51.9	640/768	-15.43 ± 7.66	-	-
$0 < G < 17$						
29	0	-30.6 ± 5.5	12/12	-	-	-
$17 < G < 22.5$, magnitude corrected according to Eq. 4						
30	0	-11.8 ± 3.0	12/12	-	-	-
31	1	-13.1 ± 7.0	48/48	-	-	-
32	2	-12.8 ± 8.9	190/192	-	-	-
33	3	-12.4 ± 12.3	705/768	-	-	-
34	4	-13.1 ± 20.1	2599/3072	-	-	-
$17 < G < 22.5$, G and $(G_{\text{BP}} - G_{\text{RP}})$ corrected according to Eqs. 4-5						
35	0	-12.4 ± 3.4	12/12	-	-	-
36	1	-13.4 ± 7.3	48/48	-	-	-
37	2	-13.0 ± 9.1	190/192	-	-	-
38	3	-13.1 ± 12.2	705/768	-	-	-
39	4	-13.5 ± 19.7	2599/3072	-	-	-

Notes. The result of the fitting Eq. 3 to the QSO sample. The value for $\langle C_0 \rangle$ is the median and dispersion over all HEALPix pixels with 40 objects per pixel or more based on Monte Carlo simulations. The number of these pixels is listed in column 4.

Table 3. Example of PZPO and error over the HEALPix pixels.

HEALPix pixel	value	error	Number
0	-6.55	9.00	1308
1	-20.79	10.05	488
2	-18.46	6.86	838
3	-16.25	12.93	635
4	-28.44	15.57	592
5	-8.94	16.20	453
6	-21.67	12.68	647
7	-22.48	13.13	515
8	-27.29	8.09	956
9	-34.50	14.58	656
10	-40.48	9.50	2146
...
760	-8.36	9.88	550
761	3.38	8.43	562
762	-8.08	12.00	404
763	0.46	10.69	542
764	5.99	11.31	486
765	-9.45	8.54	776
766	11.18	9.30	591
767	-8.84	8.87	775

Notes. Example of PZPO and error over the HEALPix pixels for level 3. The files (corresponding to models 30-39 from Table 2) are available through the CDS. The file contains the HEALPix pixel number, the PZPO with error (in μas), and column 4 is the number of objects in that pixel.

Table 4. Properties of the solutions.

HEALPix level	pixels	number of ill defined pixels	range in error (μas)
0	12	0	0.63 - 1.74
1	48	0	1.16 - 10.8
2	192	0	1.99 - 41
3	768	12	3.23 - 82
4	3072	157	1.93 - 72

Notes. Column 1: HEALPix level, Column 2: total number of pixels on the Sky, Column 3: number of pixels with 0 or 1 object, Column 4: range of the error in the PZPO for the pixels with 40 or more objects,

and that for a given π_p there are many more objects with $\pi_s < \pi_p$ than the inverse.

Restricting the magnitudes to less than 19 mag seems to largely remove this asymmetric behaviour (top panel Fig. 6) and also removes the unexpected tendency of the parallax difference as a function of magnitude (bottom panel).

It is now possible to iteratively study the PZPO based on WBs as a function of G magnitude. The first step is to correct the parallaxes according to Eq. 4. As the G magnitude of the binary sample is limited to $G = 19$ mag this implies correcting the parallaxes of all objects with $G > 17$ by $+6.0 \mu\text{as}/\text{mag}$. One can then plot the parallax difference against magnitude, only considering secondaries fainter than 17 mag. The top panel of Fig. 7 shows the result. The PZPO is essentially independent of G at the faint end, the weighted mean of the 11 bins fainter than 17.1 mag is $1.6 \pm 0.6 \mu\text{as}$. In the range between ~ 13.3 and ~ 17 mag the PZPO can be well approximated by a linear behaviour as indicated by the black line. In a second step this offset can be applied as well in this magnitude range, and the PZPO can be determined us-

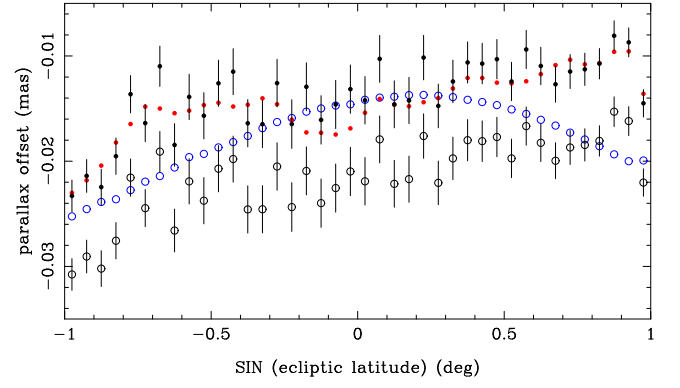


Fig. 4. PZPO for the QSO sample with $G > 17$ mag as a function of $\sin \beta$. Black open circles represent the observed data (the weighted mean) to be compared to the blue open circles that represents the L20 correction (the unweighted mean as the L20 correction carries no error). The black filled circles represent the corrected parallax data (according to Eq. 4) to be compared to the red filled circles that represent the spatial correction at $G = 20$ mag at HEALPix level 2 (both are weighted means, but the error in the red filled circles is too small to be visible).

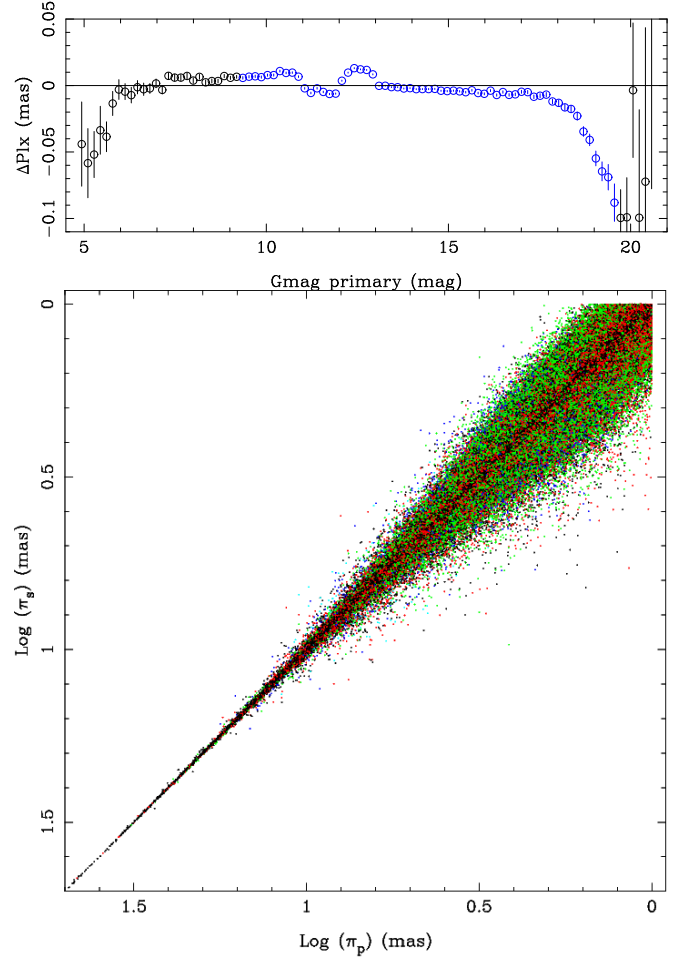


Fig. 5. Top panel. Parallax difference between primary and secondary component in wide binaries, as a function of primary G magnitude. Bins with more than 1000 objects are plotted in blue. Bottom panel. Parallax of the secondary binary component plotted against that of the primary. Objects with primary G magnitude larger than 5, 15, 17, 19, and 20 mag are plotted as black, red, green, dark blue, and light blue dots, respectively. Plotted are about 590 000 binaries where both components pass the criteria on GOF and RUWE.

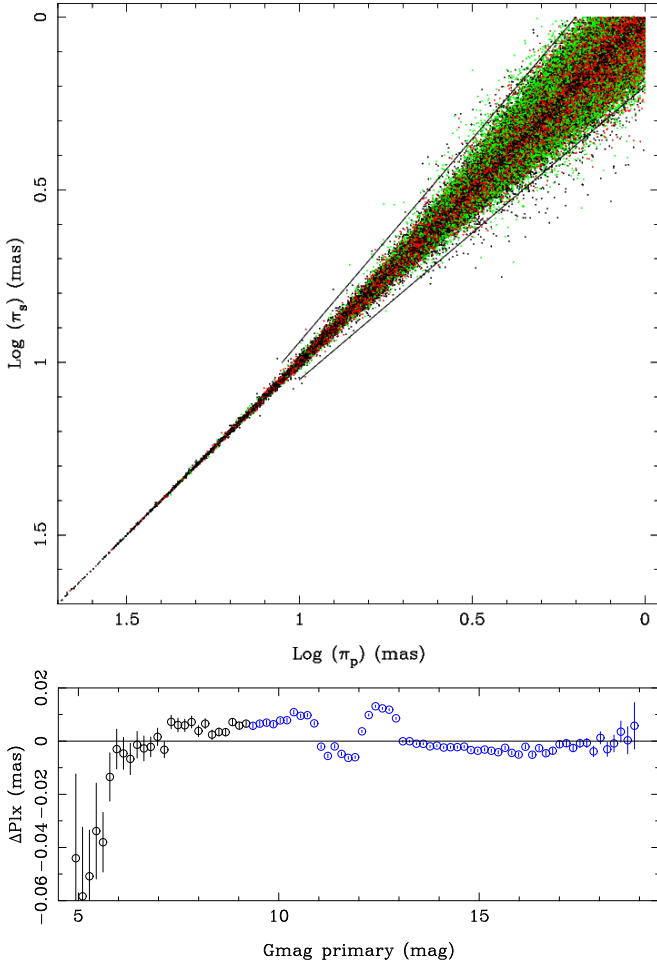


Fig. 6. As Fig. 5 for G_s restricted to < 19.0 mag. After eliminating ~ 700 extreme outliers (those outside the two plotted lines in the top panel), a sample of about 480 000 objects remain. The bottom panel shows the parallax difference between primary and secondary component for that sample as a function of G_p . Note the different range in the ordinate compared to Fig. 5.

ing secondaries fainter than 13.3 mag. The consecutive panels in Fig. 7 show how this procedure can be applied to brighter and brighter magnitudes. The bottom panel shows the final result. The weighted mean of the residuals is $0.05 \mu\text{as}$ with an rms of $2.7 \mu\text{as}$ (for $G > 6$), $4.3 \mu\text{as}$ (for $G > 5$), and $13 \mu\text{as}$ (for $5 < G < 6$ mag). The corrections that were applied with the range of G magnitudes determined so that the correction is continuous in G is given by Eq. 6. It is shown as the black line in the bottom panel.

The bottom panel of Fig. 7 also shows for comparison the correction by L20 for $\nu_{\text{eff}} = 1.55$ (corresponding to $(G_{\text{BP}} - G_{\text{RP}}) = 0.8$ mag) and $\beta = 0^\circ$ (small black circles), $+60^\circ$ (green), and -60° (red circles). The behaviour for $\beta = 0^\circ$ of the L20 correction is very similar in shape and amplitude to the correction derived here. There is an offset due to the fact that the L20 corrections are absolute while the corrections in Eq. 6 are relative to the correction at $G = 20$ which is $\approx -12.6 \mu\text{as}$ (see Table 2) which is indeed about the difference at the faint end. What is remarkable is that the L20 correction also depends in a particular way on ecliptic latitude. For bright magnitudes the L20 correction for -60° lies above that for $+60^\circ$, while for $G \gtrsim 13$ mag it

is the inverse. In addition, the dependence on β increases with brighter magnitudes.

$$\Delta\pi = \begin{cases} +6.0 (G - 19.900) + 0.000 & 16.450 \leq G < 19.900 \\ +1.78 (G - 13.265) - 26.372 & 13.218 \leq G < 16.450 \\ -40.2 (G - 12.755) - 7.823 & 12.761 \leq G < 13.218 \\ & -8.064 & 12.243 \leq G < 12.761 \\ +42.3 (G - 11.735) - 29.531 & 11.713 \leq G < 12.243 \\ -17.2 (G - 10.545) - 10.366 & 10.591 \leq G < 11.713 \\ +1.26 (G - 6.295) - 16.579 & 6.162 \leq G < 10.591 \\ +57.3 (G - 5.275) - 67.589 & 5.275 \leq G < 6.162 \end{cases} \quad (6)$$

As error in this parallax correction a $1 \mu\text{as}$ systematic error is added in quadrature to a random error of $2.7 \mu\text{as}$ for $G > 6$ and $13 \mu\text{as}$ for $G \leq 6$.

5. Application of the PZPO correction

In this section the results are being discussed related to the application of the PZPO correction.

5.1. QSOs

The first application of the PZPO correction is to the QSO sample itself and a comparison to using the L20 correction. Table 5 provides the L20 correction, and the spatial, magnitude and total correction in the present work, as well as the offset after applying the L20 correction and the correction in the present work for the different HEALPix levels. The weighted mean and the error therein are quoted in all cases. As the L20 correction comes without an error one has been assigned. It has been chosen to be a constant such that the error in the weighted mean of the L20 and the correction in the present work (Cols 2 and 5) are the same for HEALPix level 0 and equals $3.0 \mu\text{as}$. This choice has no practical impact. The error in the weighted mean after applying the corrections (Cols 6 and 7) is independent of this choice, and is actually virtually the same for both type of corrections ($\sim 0.3 \mu\text{as}$), as this error is dominated by the error in the observed parallaxes.

The results in Table 5 give the overall comparison for ~ 821 000 QSOs in the sample, but as the main difference between the approach in L20 and in the present work is in the dependence of the correction on sky position this dependence is of interest. Figure 8 shows the corrected parallax after applying the correction in the present work (in black) and that in L20 (in blue) using 60 bins in $\sin\beta$. The black points tend to be closer to the line of zero offset and Table 6 contains the details for the different HEALPix levels. The table lists the median over the bins and the scatter around the median (calculated as $1.4826 \cdot \text{MAD}$), and shows that the scatter decreases with increasing spatial resolution when using the present correction. As shown in the next two subsections, this, will not be the case in general however. As the sample to define the spatial correction is the same as to which it is applied there are no undefined spatial pixels being used. In general, increasing the spatial resolution (increasing the HEALPix level) will lead to an increasing number of stars to be in spatial pixels that are undefined (insufficient number of QSOs), so that there will be an optimal HEALPix level to be used.

Table 5. Parallax corrections for the QSO sample

HEALPix level	L20 correction (μas)	PW spatial correction (μas)	PW magnitude correction (μas)	PW total correction (μas)	$\Delta(\text{PZPO corrected}$ parallax, L20) (μas)	$\Delta(\text{PZPO corrected}$ parallax, PW) (μas)
0	-17.11 ± 0.0034	-13.49 ± 0.0010	-5.04 ± 0.0032	-18.66 ± 0.0034	-0.502 ± 0.295	$+0.008 \pm 0.295$
1	-17.11 ± 0.0034	-13.25 ± 0.0019	-5.04 ± 0.0032	-18.73 ± 0.0038	-0.502 ± 0.295	$+0.016 \pm 0.295$
2	-17.11 ± 0.0034	-13.31 ± 0.0036	-5.04 ± 0.0032	-18.70 ± 0.0050	-0.502 ± 0.295	$+0.002 \pm 0.295$
3	-17.11 ± 0.0034	-13.38 ± 0.0070	-5.04 ± 0.0032	-18.68 ± 0.0079	-0.502 ± 0.295	-0.007 ± 0.295
4	-17.11 ± 0.0034	-14.08 ± 0.0104	-5.04 ± 0.0032	-19.16 ± 0.0114	-0.502 ± 0.295	$+0.005 \pm 0.296$

Notes. Column 1 gives the HEALPix level, column 2 gives the weighted mean and error of the L20 correction, columns 3-5 give the weighted mean and error for the spatial correction, the magnitude correction, and the total correction of the present work (PW), Column 6-7 give the weighted mean and error after applying the correction in L20 and of the present work, respectively.

Table 6. Parallax corrections for the QSO sample when binned against ecliptic latitude

HEALPix level	$\Delta(\text{PZPO corrected}$ parallax, L20) (μas)	$\Delta(\text{PZPO corrected}$ parallax, present work) (μas)
0	-0.82 ± 2.75	-0.086 ± 3.06
1	-0.82 ± 2.75	$+0.078 \pm 2.50$
2	-0.82 ± 2.75	-0.080 ± 2.09
3	-0.82 ± 2.75	-0.166 ± 1.80
4	-0.82 ± 2.75	-0.090 ± 1.59

Notes. Column 1 gives the HEALPix level, column 2-3 give the median and 1.4826-MAD using the L20 correction and the present work, respectively.

5.2. Independent trigonometric parallaxes

In Sect. 3.3 a sample of 111 stars with independent trigonometric parallax data was introduced (Table 1) of which 57 pass the selection on GOF and RUWE. Figure 9 compares these parallaxes to the GEDR3 ones in the top panel, while the residuals are shown in the bottom panel.

Two stars are excluded in the further analysis, VY Pyx and HD 285876. Benedict et al. (2017) mention that VY Pyx is an outlier, lying 1.19 mag of the PL-relation they derived. Adopting the *Gaia* parallax would shift this object 1.06 mag closer, and hence in agreement, with the PL-relation. Although Benedict et al. (2017) carefully analysed all steps in their procedure, it is likely that the FGS parallax is in error. For vA 645 (HD 285876) the difference between *Gaia* and FGS parallax is 20σ , much larger than one can reasonably attribute to a statistical outlier.

Figure 10 plots the residuals against G magnitude, $(G_{\text{BP}} - G_{\text{RP}})$ colour and $\sin\beta$. Although these are the objects with the best independent trigonometric parallaxes the error bars on the differential parallax are dominated by the error in the external parallax and the range in the ordinate (~ 4 mas) is much larger than when intercomparing GEDR3 parallaxes where differences in parallax due to sky position, magnitude and colour are of order 100 times smaller (~ 0.04 mas, e.g. Figs. 3 or 7). This is probably the reason that no trends are obvious.

Table 7 gives the median and weighted mean with error of the difference between observed and the independent trigonometric parallax. The first five entries are for the entire sample applying increasingly stricter selection criteria. The last two entries are specifically for the CCs, Type-II cepheids (T2C) and RRL stars in the sample. These objects are of special interest to the distance scale, and they are all radially pulsating stars of similar magni-

tude ($7 \lesssim G \lesssim 10$) and colour ($0.5 \lesssim (G_{\text{BP}} - G_{\text{RP}}) \lesssim 2.3$ mag). Appendix A gives some more details on this subsample.

Table 8 provides the spatial, magnitude and total correction, as well as the offset between the corrected GEDR3 and independent trigonometric parallaxes. This is done for three representative samples, and for the different HEALPix levels. Ideally, the weighted mean of the difference between the corrected GEDR3 parallax and the independent trigonometric parallax (Col. 5) should be zero within the error bars, and this is indeed the case. However, some trends are observed. For the larger HEALPix levels an increasing number of stars will be missing and this results in a marked increase in the scatter. On the other hand one should favour the best mapping of the spatial variations. For the samples discussed here this would imply using the results for HEALPix level 2 as the most appropriate. However this choice will depend on the properties of the external sample (number of stars, distribution on the sky, accuracy of the external parallaxes).

5.3. Classical cepheids

As a second application of the spatial and magnitude corrections derived in the present paper the sample of Galactic CCs of Riess et al. (2021) is studied. They discuss a sample of 75 CCs with HST photometry which is used to calibrate the extragalactic distance scale along the lines outlined in earlier works (Riess et al. 2016, 2018b, 2019). They correct the GEDR3 parallaxes using the L20 formalism and fit the slope, zero point and metallicity dependence of the PL relation as well as a constant offset between the photometric parallaxes and the corrected GEDR3 values. Fits where some of these parameters are fixed are also presented. In their analysis they increased the GEDR3 parallax uncertainties by 10%, which is not done here. One important conclusion in the present context is that Riess et al. (2021) find that the L20 procedure over corrects the PZPO by $14 \pm 6 \mu\text{as}$.

Table 9 contains the result of the calculations for two samples. The first is the sample of 66 stars retained by Riess et al. (2021). This is the full sample of 75 stars minus 9 stars excluded in their best fit analysis. Six were excluded there because their GOF > 12.5 (SV Per, RW Cam, U Aql, DL Cas, SY Nor, RX Cam), one, CY Aur, because it is an outlier in the L20 correction, and S Vul and SV Vul that are marginal outliers of the PL-

Table 7. PZPOs for the sample with independent trigonometric parallaxes

median (μas)	weighted mean and error (μas)	N	description
-39	-35 ± 14	57	all that pass the GOF/RUWE selection
-39	-45 ± 14	55	excluding VY Pyx and vA 645 (10σ outliers)
-45	-71 ± 14	53	excluding 8σ outliers
-39	-36 ± 14	46	excluding 6σ outliers
-39	-39 ± 14	39	excluding 6σ outliers, $\sigma_\pi < 0.4$ mas
-33	-31 ± 16	15	all CCs, T2C, RRL that pass the GOF/RUWE selection (and excluding VY Pyx as well)
-33	-29 ± 16	13	as above, excluding Polaris B and FF Aql as well

Notes. Columns 1 and 2 list the median and weighted mean offset between the GEDR3 parallax and the independent trigonometric parallax for the sample discussed in Sects. 3.3 and 5.2. Column 3 lists the number of stars, and column 4 gives a description of the selection criteria.

Table 8. Parallax corrections for the sample with independent trigonometric parallaxes

HEALPix level	spatial correction (μas)	magnitude correction (μas)	total correction (μas)	Δ (PZPO corrected parallax) (μas)	N
Sample: 55 stars that pass GOF/RUWE selection					
0	-13.18 ± 0.14	-17.47 ± 0.40	-30.10 ± 0.44	-11.17 ± 13.88	54
1	-14.67 ± 0.29	-17.47 ± 0.40	-32.11 ± 0.53	-13.03 ± 13.93	54
2	-13.60 ± 0.58	-17.47 ± 0.40	-32.07 ± 0.78	-7.69 ± 14.16	54
3	-10.72 ± 1.12	-17.58 ± 0.41	-30.35 ± 1.26	$+2.46 \pm 18.63$	53
4	-16.11 ± 1.46	-18.07 ± 0.44	-35.74 ± 1.65	$+2.40 \pm 23.03$	45
Sample: 39 stars that pass GOF/RUWE selection, excluding 6σ outliers, $\sigma_\pi < 0.4$ mas					
0	-13.67 ± 0.19	-16.68 ± 0.48	-29.50 ± 0.53	-4.86 ± 14.50	38
1	-14.94 ± 0.37	-16.68 ± 0.48	-31.55 ± 0.65	-6.85 ± 14.55	38
2	-13.98 ± 0.75	-16.68 ± 0.48	-31.95 ± 0.99	-2.16 ± 14.81	38
3	-12.58 ± 1.53	-16.81 ± 0.49	-31.56 ± 1.70	$+13.81 \pm 20.16$	37
4	-25.05 ± 1.94	-17.58 ± 0.54	-43.10 ± 2.24	-4.42 ± 25.71	30
Sample: 13 CCs, T2C, RRL					
0	-13.91 ± 0.35	-13.47 ± 0.80	-26.72 ± 0.88	-6.75 ± 15.91	13
1	-14.49 ± 0.70	-13.47 ± 0.80	-27.49 ± 1.12	-2.87 ± 15.97	13
2	-14.31 ± 1.41	-13.47 ± 0.80	-28.13 ± 1.85	$+3.92 \pm 16.30$	13
3	-10.48 ± 3.19	-13.47 ± 0.80	-24.47 ± 3.56	$+2.70 \pm 23.70$	13
4	-7.38 ± 5.54	-12.95 ± 1.01	-20.13 ± 5.79	$+16.91 \pm 32.86$	8

Notes. Column 1 gives the HEALPix level considered (defining the spatial correction term), columns 2-5 give the weighted mean and error for the spatial correction, the magnitude correction, the total correction, and the offset between the corrected GEDR3 parallax and the external parallax. Column 6 gives the number of stars. The samples refer to those defined in Tab. 7.

relation³. The second sample are the 54 stars that remain after the applying the criteria on GOF and RUWE used in this paper.

The reference parallax is the photometric parallax (with error) from Table 1 in Riess et al. (2021) that is derived from the HST photometry, the pulsation period, and the PL relation from Riess et al. (2016, 2019).

Column 2 of Tab. 9 gives the weighted mean offset between the observed GEDR3 parallax and the photometric parallax. It is unusually large (-6.4 to $-7.7 \mu\text{as}$, see below). Column 3 lists the weighted mean of the L20 correction, and the upper panel of Fig. 11 show the dependence on β . A similar diagram was shown for the 75 CCs in Riess et al. (2021). What is striking is the close to parabolic shape of the correction which is build-in in

the L20 approach. The other columns show the weighted mean spatial, magnitude, and total correction, the offset between the corrected GEDR3 parallax and the photometric parallax, and the number of objects. If the GEDR3 parallaxes are corrected by the L20 formalism (on a star-by-star basis) the weighted mean offset with the photometric parallax becomes $+14.3 \pm 2.9 \mu\text{as}$, consistent with Riess et al. (2021), and indicating an overcorrection by the L20 formalism. By increasing the photometric parallaxes by $\sim 3.3\%$ one can obtain a weighted mean offset between the L20 corrected and photometric parallax consistent with zero ($0.00 \pm 2.93 \mu\text{as}$). Such an increase is consistent with the result reported in the last entry of table 2 in Riess et al. (2021) where they forced a fit without additional PZPO to determine the zero point of the PL relation. The value reported there (-5.865 ± 0.013) is consistent with finding here that implies a zero point of $-5.93 + 5 \log 1.0325 = -5.861$.

The second block in Table 9 shows similar results for the smaller sample that fulfils the criteria on GOF and RUWE im-

³ It was confirmed (Riess 2021, private communication) that two corrections are necessary in Table 1 of Riess et al. (2021) to match their analysis; Z Sct is missing there but is available in Table 1 of Riess et al. 2018b, and the high GOF flag on AD Pup (GOF = 12.48) should instead appear on RX Cam (GOF = 28.7).

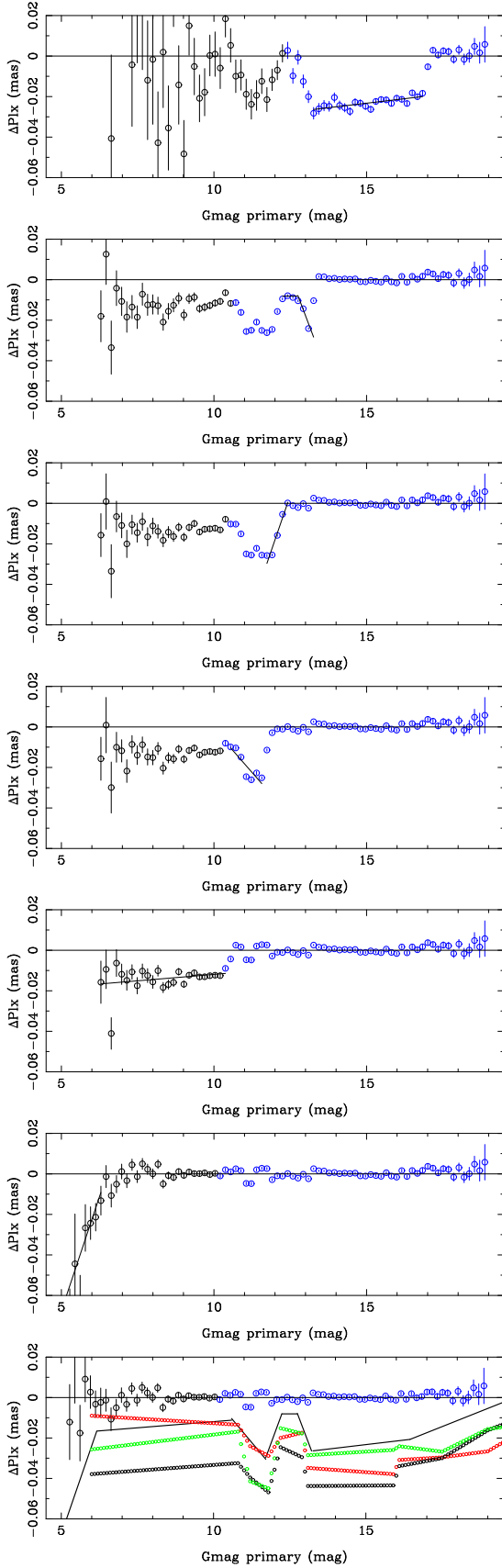


Fig. 7. As Fig. 5 with parallaxes corrected according to Eq. 6 in consecutive steps (see main text). The bottom panel shows the applied correction (Eq. 6) as the black line. The small black, red, and green circles represent the L20 correction for $\beta = 0, -60$, and $+60^\circ$. There is an offset as the L20 corrections are absolute, while the corrections applied to the WB sample are relative to the correction at $G = 20$ mag.

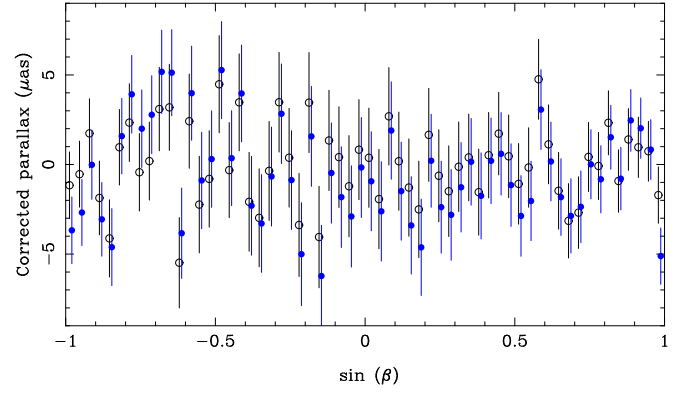


Fig. 8. Residual in the observed parallax after applying the correction in the present work (in black open circles, offset by -0.004 units horizontally) and that in L20 (in blue filled circles, offset by $+0.004$ units) versus $\sin\beta$ for the QSO sample. Sixty bins have been used, and HEALPix level 2 has been used in the calculations.

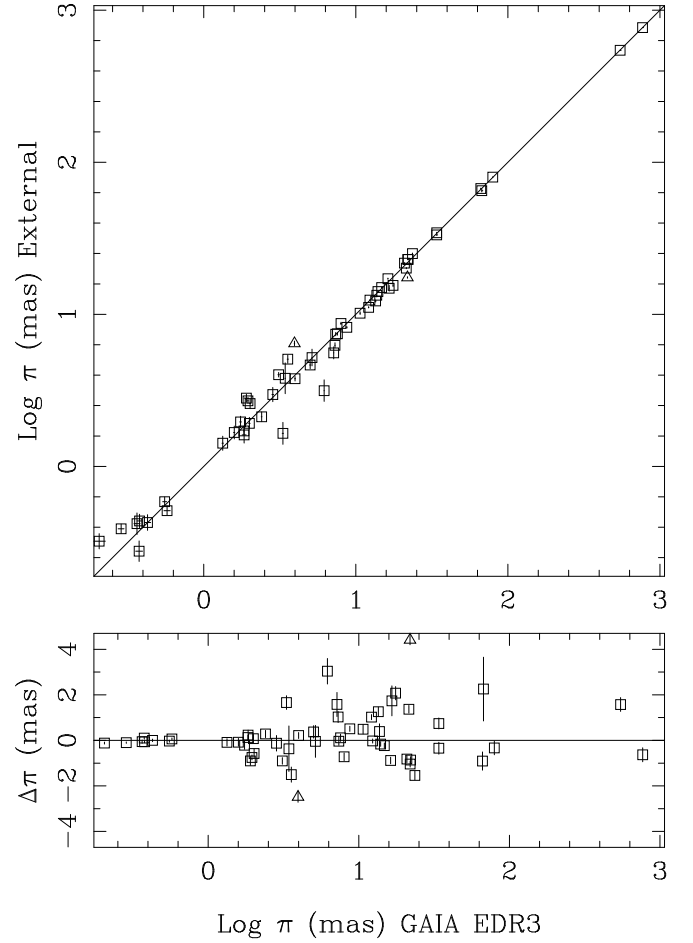


Fig. 9. Independent trigonometric parallax plotted against GEDR3 parallax. The bottom panel displays the residual, where the error bar in the ordinate combines the error in the *Gaia* and the independent parallax in quadrature. Two stars where the residual is more than ten times the combined error bar are plotted as open triangles.

posed here. The bottom panel of Fig. 11 shows that there is no the dependence of the total correction (with error bar) proposed in the present paper on β . It is remarked that the error in the average total correction (Col. 6) is similar or smaller than the average L20 correction (Col. 3) for HEALPix levels 0, 1, and 2.

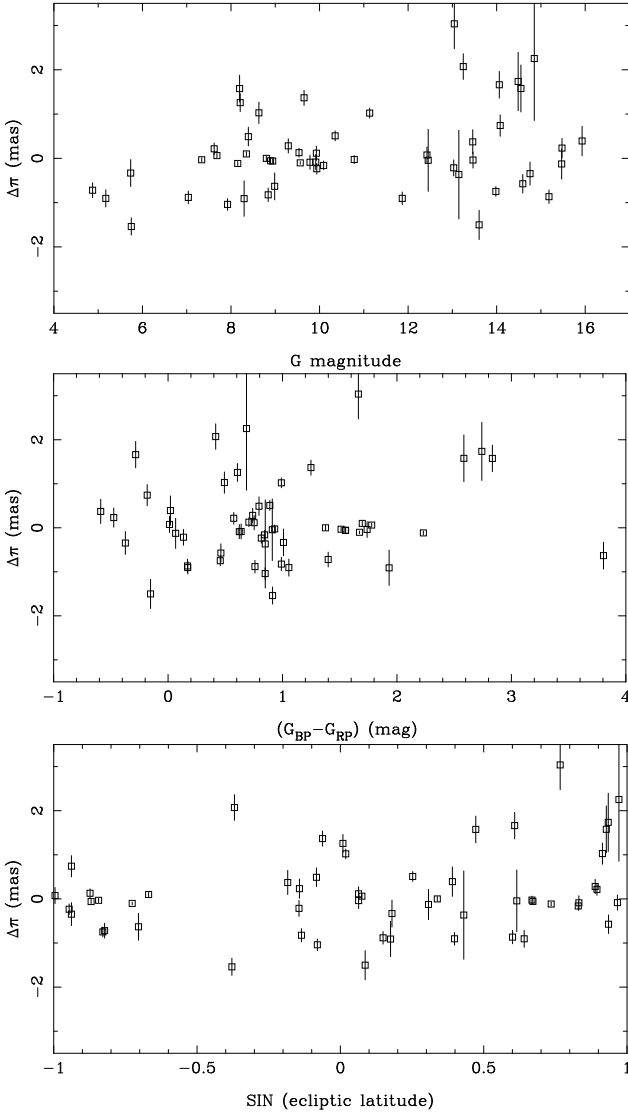


Fig. 10. Difference between the independent trigonometric parallax and the GEDR3 parallax plotted against G , $(G_{BP} - G_{RP})$ colour, and $\sin\beta$. The two outliers mentioned in Fig. 9 have been removed.

Adopting the standard photometric parallax leads to overcorrection of $\sim 20 \mu\text{as}$. Increasing the photometric parallax by a factor 1.0505 ± 0.0080 (implying a PL zero point of -5.823 ± 0.016 , and $H_0 = 76.2 \pm 1.3 \text{ km/s/Mpc}$) will lead to weighted mean offset between the corrected GEDR3 and the photometric parallax consistent with zero. It also implies a weighted mean offset of the observed GEDR3 and the photometric parallax of $-29 \pm 3 \mu\text{as}$, which is very similar to other bright ($G \lesssim 10\text{--}11 \text{ mag}$) samples, for example the stars with external trigonometric parallaxes and the subsample of pulsating stars (-39 ± 14 , respectively, $-29 \pm 16 \mu\text{as}$ from Tab. 7) or the sample of EBs ($-37 \pm 20 \mu\text{as}$, Stassun & Torres 2021) or WUMa-type EBs ($-28.6 \pm 0.6 \mu\text{as}$ for the 5-parameter solution, Ren et al. 2021).

6. Discussion and summary

The presence of a parallax zero point offset that was identified in GDR2 received a lot of attention. The L20 paper analysing the new GEDR3 data offers a lot of insight into the issue and they presented a python script to calculate the correction

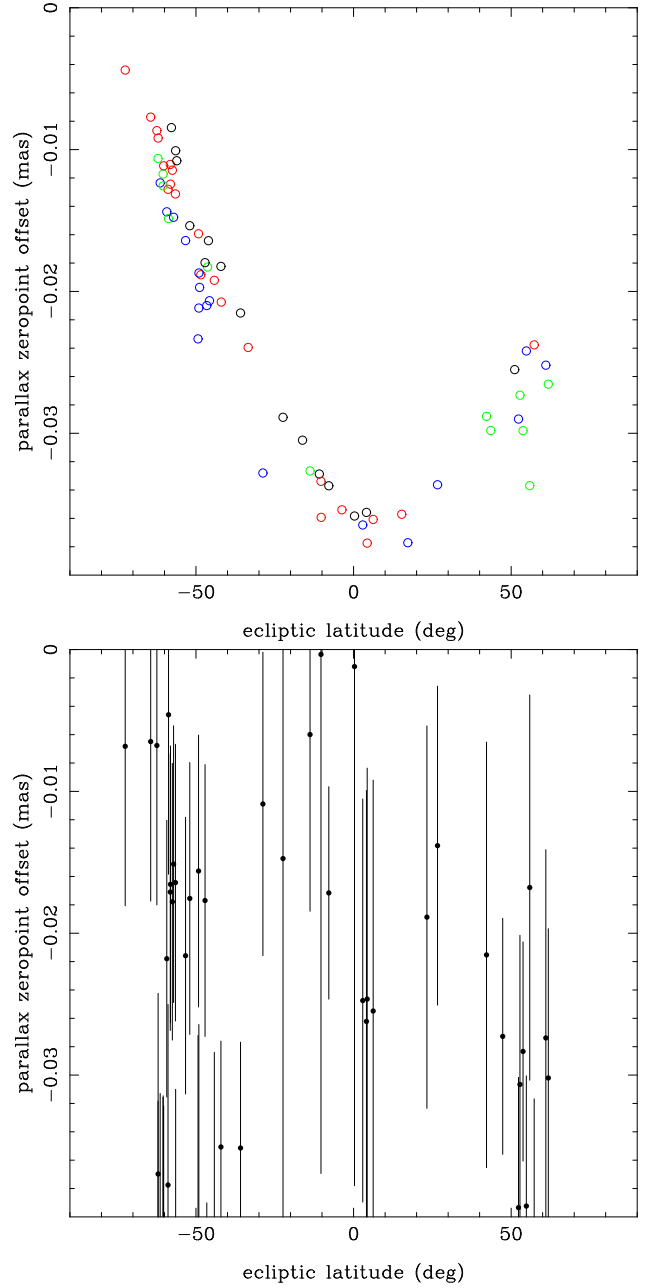


Fig. 11. Top panel: PZPO correction by L20 for the sample of 66 CCs analysed by Riess et al. (2021) (cf. their Fig. 2). The colours represent different ranges in G : black ($G \leq 7$), red ($7 < G \leq 8.5$), green ($8.5 < G \leq 9.0$), and blue ($9 < G \leq 11.5$). Bottom panel: Correction proposed here for the stricter selected sample of 54 stars at HEALPix level 2.

based on G , β , and the pseudocolour or ν_{eff} (depending on the `astrometric_params_solved` parameter).

On the other hand, L20 remark that ‘the results should ... in no way be regarded as definitive’, and that ‘alternative routes are explored towards getting a better handle on the systematics in Gaia data’. The present paper should be viewed in this light. An alternative procedure to the one in L20 is proposed which is offered to the community for further scrutiny.

The two approaches are similar in that both use samples of QSOs and wide binaries (albeit selected in different ways). The main differences to the L20 approach are that (1) there is no separation between 5- and 6-parameter solutions, (2) the colour dependence uses the $(G_{BP} - G_{RP})$ colour rather than pseudocolour

Table 9. Parallax corrections for samples of Galactic CCs

HEALPix level	$\Delta(\text{uncorrected parallax})$ (μas)	L20 correction (μas)	PW spatial correction (μas)	PW magnitude correction (μas)	PW total correction (μas)	$\Delta(\text{PZPO corrected parallax, PW})$ (μas)	N	Remarks
66 CCs following Riess et al. (2021)								
0	-6.36 ± 2.83	-22.1 ± 1.23	-14.10 ± 0.17	-14.55 ± 0.35	-27.82 ± 0.39	$+22.0 \pm 2.87$	66	
1			-14.13 ± 0.38	-14.55 ± 0.35	-27.57 ± 0.55	$+20.3 \pm 2.90$	66	
2			-14.43 ± 1.25	-14.55 ± 0.35	-28.94 ± 1.31	$+25.1 \pm 3.26$	66	
3			-10.43 ± 4.12	-14.57 ± 0.36	-25.34 ± 4.17	$+17.4 \pm 6.73$	63	
4			-8.58 ± 8.57	-14.67 ± 0.47	-23.90 ± 8.64	$+24.7 \pm 11.5$	38	
2	-20.5 ± 2.83		-14.43 ± 1.25	-14.55 ± 0.35	-28.94 ± 1.31	$+10.4 \pm 3.26$	66	$\pi_{\text{phot}} \cdot 1.0325^a$
54 CCs following the GOF/RUWE selection in the present work								
0	-7.66 ± 3.04	-22.0 ± 1.36	-13.66 ± 0.19	-14.54 ± 0.39	-27.39 ± 0.44	$+20.4 \pm 3.08$	54	
1			-13.51 ± 0.42	-14.54 ± 0.39	-27.15 ± 0.60	$+18.5 \pm 3.12$	54	
2			-13.57 ± 1.41	-14.54 ± 0.39	-28.04 ± 1.47	$+22.2 \pm 3.53$	54	
3			-8.05 ± 4.66	-14.57 ± 0.40	-22.70 ± 4.73	$+13.4 \pm 7.62$	51	
4			-6.94 ± 9.24	-14.82 ± 0.55	-22.35 ± 9.32	$+22.7 \pm 12.7$	27	
2	-29.2 ± 3.05		-13.57 ± 1.41	-14.54 ± 0.39	-29.22 ± 3.05	$+0.00 \pm 3.53$	54	$\pi_{\text{phot}} \cdot 1.0505$

Notes. Column 1 gives the HEALPix level considered (defining the spatial correction term), column 2 gives the weighted mean and error of the offset between the observed GEDR3 parallax and the photometric parallax, column 3 gives the weighted mean and error of the L20 correction, columns 4-7 give the weighted mean and error for the spatial correction, the magnitude correction, the total correction, and the offset between the corrected GEDR3 parallax in the present work (PW) and the photometric parallax. Column 8 gives the number of stars. The sample sizes of 66 and 54 stars are explained in Sect. 5.3. ^(a) This model results in a $\Delta(\text{PZPO corrected parallax})$ of $0.00 \pm 2.93 \mu\text{as}$ when using the L20 correction.

or ν_{eff} , (3) the dependence on sky position and magnitude are separated, and are treated as additive terms, and that (4) the present approach gives a correction including an error estimate.

It is shown that the PZPO shows a more complicated behaviour than only on the ecliptic latitude (Fig. 3, also see Huang et al. 2021). L20 argue that such a dependence is theoretically expected and related to the scanning law but this would not explain the different behaviour at bright (Fig. 11; a range of $\sim 35 \mu\text{as}$ with the largest correction around $\beta \sim 5^\circ$) and faint magnitudes (Fig. 4; a range of $\sim 20 \mu\text{as}$ with a slow increase with β) in the L20 recipe.

Here, the practical approach is taken to calculate the PZPO over the sky using the HEALPix formalism. Using the dependence of the PZPO as a function of G , a spatial PZPO at $G = 20$ mag is determined for several HEALPix levels, based on the QSO sample for $G > 17$ mag. A large sample of WBs with very low chance alignments is used to derive the magnitude dependence of the PZPO for magnitudes < 19 mag. The range of $17 - 19$ mag is used to connect the QSO to the WB sample.

The L20 recipe does not provide an error on the correction. It is shown here that error on the PZPO is dominated by the error on the spatial correction, and that it can be substantial (up to several tens of μas depending on sky position). Increasing the sample of QSOs, especially in the direction of the Galactic plane, will help in reducing the statistical error but only as $1/\sqrt{N}$.

The recipes provided here can not be easily transformed into a simple script. This may be seen as a disadvantage, on the other hand it requires the user to make informed choices. The procedure to be followed is as follows:

- Obtain the `source_id`, G magnitude, parallax and error, and $(G_{\text{BP}} - G_{\text{RP}})$ colour from GEDR3 for your source(s).
- Get the pixel number in the HEALPix scheme from the `source_id` following footnote 2 for levels 0, 1, 2, 3, and 4.

- Use the results from models 30-34 available from the CDS to obtain the spatial correction and error at $G = 20$ for the various HEALPix levels.
- For $G > 19.9$ mag apply Eq. 4, otherwise apply Eq. 6. The error in this correction is a $1 \mu\text{as}$ systematic error to be added in quadrature to a random error of $2.7 \mu\text{as}$ for $G > 6$ and $13 \mu\text{as}$ for $G \leq 6$.
- If a colour term is to be included use the results from models 35-39, and additionally apply Eq. 5. This colour term is derived for the QSOs sample ($G \gtrsim 17$ mag, $0.2 \lesssim (G_{\text{BP}} - G_{\text{RP}}) \lesssim 1.6$ mag) and is untested outside this range.
- Add the spatial and magnitude (+colour) correction, and add the errors in quadrature. Subtract the total from the observed parallax to obtain the corrected parallax, that is, an estimate of the true parallax (Eq. 1). Also in this last step the errors should be added in quadrature.

Following the examples described in Section 5, it is recommended to do this for all available HEALPix levels and then choose the highest level that does not compromise the S/N.

Acknowledgements. This work has made use of data from the European Space Agency (ESA) mission *Gaia* (<https://www.cosmos.esa.int/gaia>), processed by the *Gaia* Data Processing and Analysis Consortium (DPAC, <https://www.cosmos.esa.int/web/gaia/dpac/consortium>). Funding for the DPAC has been provided by national institutions, in particular the institutions participating in the *Gaia* Multilateral Agreement. This research has made use of the SIMBAD database, the VizieR catalogue access tool and the cross-match service provided by CDS, Strasbourg. Thanks to Francois-Xavier Pineau for explaining the best use of the cross-match service. Some of the results in this paper have been derived using the *healpy* and *HEALPix* package. I would like to thank Drs. Kareen El-Badry and Valentin Ivanov for discussions on wide binaries and quasar catalogues, respectively, and the referee for a careful reading of the manuscript and helpful suggestions.

References

Anderson, R. I. 2018, *A&A*, 611, L7

- Benedict, G. F., McArthur, B. E., Nelan, E. P., & Harrison, T. E. 2017, *PASP*, 129, 012001
- Bhardwaj, A., Rejkuba, M., de Grijs, R., et al. 2021, *ApJ*, 909, 200
- Bond, H. E., Nelan, E. P., Remage Evans, N., Schaefer, G. H., & Harmer, D. 2018, *ApJ*, 853, 55
- Casertano, S., Riess, A. G., Anderson, J., et al. 2016, *ApJ*, 825, 11
- Chan, V. C. & Bovy, J. 2020, *MNRAS*, 493, 4367
- Clementini, G., Ripepi, V., Molinaro, R., et al. 2019, *A&A*, 622, A60
- El-Badry, K., Rix, H.-W., & Heintz, T. M. 2021, *MNRAS*[arXiv:2101.05282]
- Fabricius, C., Luri, X., Arenou, F., et al. 2021, *A&A*, 649, A5
- Flesch, E. W. 2019, arXiv e-prints, arXiv:1912.05614
- Gaia Collaboration, Brown, A. G. A., Vallenari, A., et al. 2018, *A&A*, 616, A1
- Gaia Collaboration, Brown, A. G. A., Vallenari, A., et al. 2021a, *A&A*, 649, A1
- Gaia Collaboration, Klioner, S. A., Mignard, F., et al. 2021b, *A&A*, 649, A9
- Gaia Collaboration, Prusti, T., de Bruijne, J. H. J., et al. 2016, *A&A*, 595, A1
- Górski, K. M., Hivon, E., Banday, A. J., et al. 2005, *ApJ*, 622, 759
- Graczyk, D., Pietrzyński, G., Gieren, W., et al. 2019, *ApJ*, 872, 85
- Groenewegen, M. A. T. 2018, *A&A*, 619, A8
- Huang, Y., Schönrich, R., Zhang, H., et al. 2020, *ApJS*, 249, 29
- Huang, Y., Yuan, H., Beers, T. C., & Zhang, H. 2021, *ApJ*, 910, L5
- Khan, S., Miglio, A., Mosser, B., et al. 2019, in *The Gaia Universe*, 13
- Layden, A. C., Tiede, G. P., Chaboyer, B., Bunner, C., & Smitka, M. T. 2019, *AJ*, 158, 105
- Leung, H. W. & Bovy, J. 2019, *MNRAS*, 489, 2079
- Lindgren, L. 2018, *GAIA-C3-TN-LU-LL-124*
- Lindgren, L., Bastian, U., Biermann, M., et al. 2021a, *A&A*, 649, A4
- Lindgren, L., Hernández, J., Bombrun, A., et al. 2018, *A&A*, 616, A2
- Lindgren, L., Klioner, S. A., Hernández, J., et al. 2021b, *A&A*, 649, A2
- Muraveva, T., Delgado, H. E., Clementini, G., Sarro, L. M., & Garofalo, A. 2018, *MNRAS*, 481, 1195
- Press, W., Teukolsky, S., Vetterling, W., & Flannery, B. 1992, *Numerical Recipes in C* (Cambridge: Cambridge University Press)
- Ren, F., Chen, X., Zhang, H., et al. 2021, *ApJ*, 911, L20
- Riess, A. G., Casertano, S., Anderson, J., MacKenty, J., & Filippenko, A. V. 2014, *ApJ*, 785, 161
- Riess, A. G., Casertano, S., Yuan, W., et al. 2021, *ApJ*, 908, L6
- Riess, A. G., Casertano, S., Yuan, W., et al. 2018a, *ApJ*, 855, 136
- Riess, A. G., Casertano, S., Yuan, W., et al. 2018b, *ApJ*, 861, 126
- Riess, A. G., Casertano, S., Yuan, W., Macri, L. M., & Scolnic, D. 2019, *ApJ*, 876, 85
- Riess, A. G., Macri, L. M., Hoffmann, S. L., et al. 2016, *ApJ*, 826, 56
- Ripepi, V., Molinaro, R., Musella, I., et al. 2019, *A&A*, 625, A14
- Schönrich, R., McMillan, P., & Eyer, L. 2019, *MNRAS*, 487, 3568
- Stassun, K. G. & Torres, G. 2018, *ApJ*, 862, 61
- Stassun, K. G. & Torres, G. 2021, *ApJ*, 907, L33
- van Belle, G. T., Schaefer, G. H., von Braun, K., et al. 2020, *PASP*, 132, 054201
- Wilson, E. B. & Hilferty, M. M. 1931, *Proceedings of the National Academy of Science*, 17, 684
- Xu, S., Zhang, B., Reid, M. J., Zheng, X., & Wang, G. 2019, *ApJ*, 875, 114
- Zinn, J. C. 2021, *AJ*, 161, 214
- Zinn, J. C., Pinsonneault, M. H., Huber, D., & Stello, D. 2019, *ApJ*, 878, 136
- Zonca, A., Singer, L., Lenz, D., et al. 2019, *Journal of Open Source Software*, 4, 1298

Appendix A: Parallax difference for classical pulsators

Figure A.1 is as Figs. 9 and 10 for the sample of 15 CCs, T2C, and RRL stars. Two outliers are plotted as open triangles. They are FF Aql and Polaris B. FF Aql is very bright ($G = 5.1$ mag) and this may be the reason for the offset. For Polaris B the reason is less clear. The GOF (3.55) and RUWE (1.15) easily fall within the applied selection criteria. The difference between the FGS parallax for Polaris B and the *Hipparcos* parallax for Polaris A have been discussed in the literature without reaching a conclusion on its implications (Bond et al. 2018; Anderson 2018; appendix B in Groenewegen 2018).

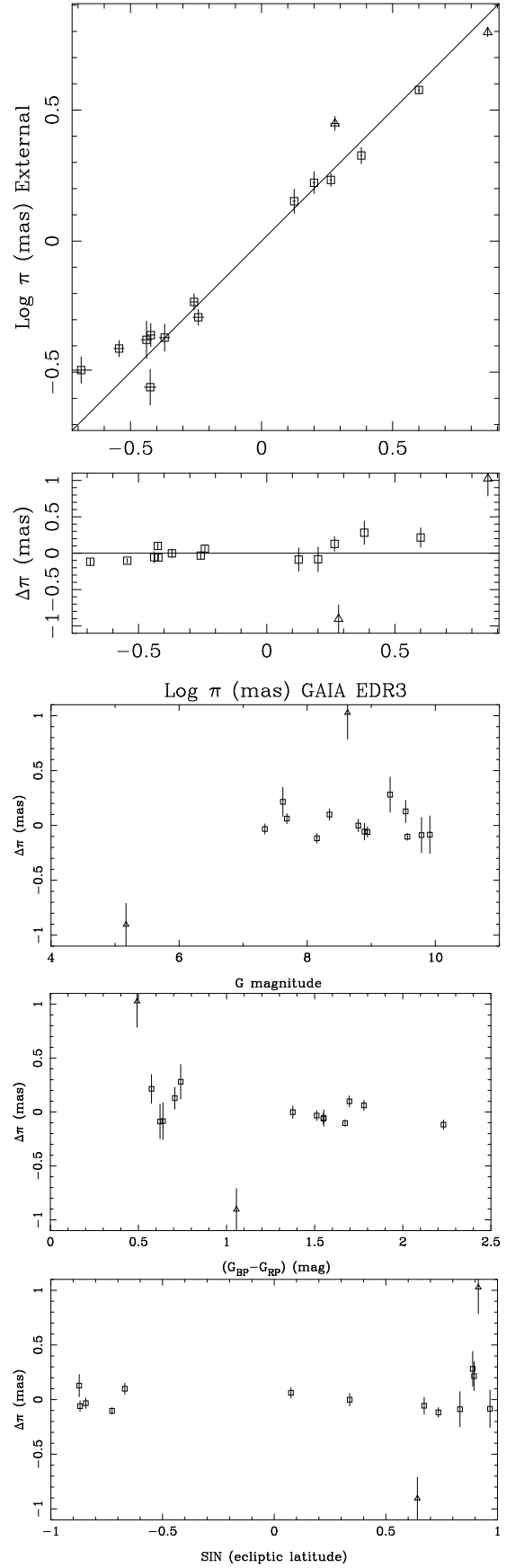


Fig. A.1. Difference between the independent trigonometric parallax and the GEDR3 parallax plotted against G , $(G_{BP} - G_{RP})$ colour, and $\sin\beta$ for the 15 CCs, T2C, and RRL stars. Two outliers are plotted as open triangles.

Table 1. Stars with independent trigonometric parallaxes, ordered by Right Ascension.

Identifier	parallax (mas)	Ref.	Ra (deg)	Dec (deg)	Source ID	parallax (mas)	GoF	RUWE	G (mag)	$(G_{BP} - G_{RP})$ (mag)
GJ1005A	166.6 \pm 0.3	1	3.869880	-16.136572	2368293487261055488		809.35		10.268 \pm 0.005	2.819 \pm 0.005
GJ22C	99.2 \pm 0.6	1	8.142840	+67.233278	527956488339113600	100.397 \pm 0.037	12.87	1.54	11.107 \pm 0.003	2.620 \pm 0.012
GJ22A	99.2 \pm 0.6	1	8.143031	+67.234328	527956488340229632	101.086 \pm 0.461	91.24	5.89	9.567 \pm 0.003	2.304 \pm 0.005
ν Aan	73.71 \pm 0.1	1	24.198321	+41.403762	348020482735930112	74.194 \pm 0.208	77.72	7.25	3.966 \pm 0.003	0.723 \pm 0.007
VX Per	0.42 \pm 0.0744	5	31.952002	+58.443534	506779550797525760	0.364 \pm 0.017	3.49	1.12	8.894 \pm 0.009	1.551 \pm 0.048
RW Tri	2.93 \pm 0.33	1	36.400769	+28.097391	130692247044752768	3.267 \pm 0.022	6.10	1.34	13.246 \pm 0.033	0.631 \pm 0.153
Polaris B	6.26 \pm 0.24	2	37.664816	+89.260830	576402619921510144	7.287 \pm 0.018	3.55	1.15	8.630 \pm 0.003	0.492 \pm 0.005
Polaris A	7.62 \pm 0.08	3	(37.967198)	(+89.264051)						
Feige 24	14.6 \pm 0.4	1	38.782009	+3.732482	2503828498910129664	12.868 \pm 0.036	11.01	1.58	12.210 \pm 0.003	0.193 \pm 0.006
REJ 0317-853	34.38 \pm 0.26	1	49.311809	-85.540486	4613612951211823104	34.035 \pm 0.029	0.69	1.02	14.754 \pm 0.004	-0.373 \pm 0.014
LB 9802	33.28 \pm 0.24	1	49.326169	-85.542124	4613612951211823616	34.021 \pm 0.019	2.49	1.09	14.079 \pm 0.003	-0.182 \pm 0.005
GK Per	2.1 \pm 0.12	1	52.799999	+43.904220	238540495056450048	2.306 \pm 0.042	48.50	3.35	12.557 \pm 0.007	1.393 \pm 0.029
ϵ Eri	311.37 \pm 0.11	1	53.228293	-9.458168	5164707970261890560	310.577 \pm 0.136	31.41	2.72	3.466 \pm 0.003	1.140 \pm 0.011
Cl* Melotte 22 HII 3030	7.41 \pm 0.18	1	57.855681	+23.889172	66481734354737792	7.371 \pm 0.018	0.47	1.02	13.465 \pm 0.003	1.739 \pm 0.007
Cl* Melotte 22 HII 3063	7.43 \pm 0.16	1	57.874842	+23.899036	66481837433947392	7.498 \pm 0.025	8.04	1.30	13.028 \pm 0.003	1.571 \pm 0.007
Cl* Melotte 22 HII 3179	7.45 \pm 0.16	1	57.987027	+23.901753	66471220274934272	7.565 \pm 0.017	2.34	1.08	9.927 \pm 0.003	0.752 \pm 0.005
XO-3	5.67 \pm 0.14	1	65.469581	+57.817210	470650560779277952	4.869 \pm 0.026	9.03	1.25	9.743 \pm 0.003	0.565 \pm 0.005
vA 310	20.13 \pm 0.17	1	66.071101	+18.002784	3314079508140198528	21.497 \pm 0.015	0.69	1.02	9.650 \pm 0.003	1.248 \pm 0.005
vA 383	21.53 \pm 0.2	1	66.520077	+15.041285	3311179340063437952	20.839 \pm 0.028	25.01	1.89	11.470 \pm 0.003	1.912 \pm 0.005
vA 472	21.7 \pm 0.15	1	67.018941	+13.867854	3307844864893938304	20.876 \pm 0.021	0.68	1.02	8.840 \pm 0.003	0.990 \pm 0.005
vA 548	20.69 \pm 0.17	1	67.379585	+16.244692	3312899491645515776	21.818 \pm 0.021	6.31	1.24	9.932 \pm 0.003	1.373 \pm 0.005
vA 622	24.11 \pm 0.3	1	67.871614	+17.718519	3314150048683152896	22.236 \pm 0.022	5.07	1.18	11.184 \pm 0.003	1.879 \pm 0.005
vA 627	21.74 \pm 0.25	1	67.905103	+17.709637	3314151251273992832	28.508 \pm 0.581	488.26	43.27	9.248 \pm 0.003	1.180 \pm 0.005
vA 645	17.46 \pm 0.21	1	67.969120	+15.499373	3312564037520033792	21.872 \pm 0.016	2.77	1.10	10.498 \pm 0.003	1.573 \pm 0.005
HD 33636	35.6 \pm 0.2	1	77.944347	+4.402925	3238810137558836352	33.798 \pm 0.053	20.84	1.88	6.865 \pm 0.003	0.750 \pm 0.005
SY Aur	0.428 \pm 0.054	4	78.163452	+42.831780	201509768065410944	0.427 \pm 0.020	2.50	1.08	8.798 \pm 0.008	1.376 \pm 0.038
TV Col	2.7 \pm 0.11	1	82.356418	-32.817651	2901783160488793728	1.951 \pm 0.014	2.96	1.10	13.981 \pm 0.011	0.456 \pm 0.050
GJ1081A	65.2 \pm 0.37	1	83.329996	+44.814683	207910437566174592		647.99		11.019 \pm 0.004	2.678 \pm 0.005
β Dor	3.14 \pm 0.16	1	83.406311	-62.489769	4757601523650165120	2.931 \pm 0.139	47.30	4.54	3.593 \pm 0.014	1.050 \pm 0.053
HD 38529	25.11 \pm 0.19	1	86.645126	+1.167567	3219847066672970368	23.571 \pm 0.042	1.31	1.05	5.748 \pm 0.003	0.913 \pm 0.005
SS Aur	5.99 \pm 0.33	1	93.343503	+47.740270	968824328534823936	3.978 \pm 0.028	15.02	1.69	14.318 \pm 0.024	0.978 \pm 0.098
RT Aur	2.4 \pm 0.19	1	97.142032	+30.492976	3435571660360952704	1.815 \pm 0.122	66.45	6.43	5.336 \pm 0.021	0.828 \pm 0.086
GJ234A	240.98 \pm 0.4	1	97.350795	-2.817131	3117120863523946368		761.25		9.630 \pm 0.005	3.080 \pm 0.012
RR Pic	1.92 \pm 0.18	1	98.900296	-62.640097	5477422099543150592	1.996 \pm 0.021	2.50	1.10	12.425 \pm 0.006	0.013 \pm 0.021
HD 47536	8.71 \pm 0.16	1	99.448976	-32.339444	5583831735369515008	7.990 \pm 0.053	-3.12	0.88	4.874 \pm 0.003	1.399 \pm 0.006
G250-029A	95.59 \pm 0.28	1	103.522633	+60.867338	1003752587430126464	91.611 \pm 0.503	130.21	9.05	10.003 \pm 0.006	2.534 \pm 0.005
G193-027A	110.2 \pm 1.1	1	105.987163	+52.697727	981548637301374336	110.826 \pm 0.695	234.89	18.90	11.699 \pm 0.003	3.210 \pm 0.005
ζ Gem	2.78 \pm 0.18	1	106.027177	+20.570294	3366754155291545344	3.073 \pm 0.218	21.96	2.78	3.540 \pm 0.006	0.987 \pm 0.030
SS CMa	0.389 \pm 0.0287	5	111.529960	-25.257297	5616601820448126336	0.286 \pm 0.013	3.97	1.11	9.563 \pm 0.007	1.673 \pm 0.032
X Pup	0.277 \pm 0.0469	5	113.195965	-20.909682	5620098679741674496	0.376 \pm 0.020	1.19	1.04	8.348 \pm 0.012	1.697 \pm 0.052
YY Gem	67.22 \pm 0.4	6	113.654977	+31.869063	892348454394856064	66.311 \pm 0.024	0.16	1.01	8.296 \pm 0.003	1.932 \pm 0.008
U Gem	9.96 \pm 0.37	1	118.771670	+22.001222	674214551557961984	10.705 \pm 0.034	31.00	2.41	13.903 \pm 0.011	1.280 \pm 0.049
ρ^1 Cnc	79.78 \pm 0.3	1	133.146761	+28.329783	704967037090946688	79.448 \pm 0.043	-3.81	0.86	5.733 \pm 0.003	1.009 \pm 0.005
PN A66 31	1.61 \pm 0.21	1	133.554806	+8.898001	597324024095840512	1.842 \pm 0.055	0.95	1.03	15.475 \pm 0.003	-0.475 \pm 0.006
VY Pyx	6.44 \pm 0.23	1	133.623514	-23.521695	5653136461526964224	3.950 \pm 0.019	-3.57	0.89	7.107 \pm 0.005	0.811 \pm 0.017
HIP 46120	15.01 \pm 0.12	1	141.092846	-80.517086	5195968563310843008	14.776 \pm 0.014	-1.60	0.94	9.938 \pm 0.003	0.814 \pm 0.005
ℓ Car	2.01 \pm 0.2	1	146.311593	-62.507867	5250032958818831360	1.984 \pm 0.110	24.35	2.39	3.471 \pm 0.014	1.503 \pm 0.047
HD 84937	12.24 \pm 0.2	1	147.235464	+13.740818	615943806835727872	13.498 \pm 0.044	1.94	1.10	8.207 \pm 0.003	0.606 \pm 0.005

Table 1. continued.

Identifier	parallax (mas)	Ref.	Ra (deg)	Dec (deg)	Source ID	parallax (mas)	GoF	RUWE	G (mag)	(G _{BP} - G _{RP}) (mag)
VY Car	0.586 ± 0.0438	5	161.136160	-57.565357	5351161399793209984	0.553 ± 0.017	-2.35	0.92	7.338 ± 0.009	1.511 ± 0.038
XY Car	0.438 ± 0.0469	5	165.566881	-64.262893	5240441472232302848	0.378 ± 0.014	2.08	1.07	8.941 ± 0.009	1.549 ± 0.043
HIP 54639	11.12 ± 0.11	1	167.747457	+6.417567	3817965105665685504	12.141 ± 0.020	2.60	1.12	11.131 ± 0.003	0.990 ± 0.005
SU Dra	1.42 ± 0.16	1	174.485330	+67.329393	1058066262817534336	1.332 ± 0.014	0.35	1.01	9.784 ± 0.012	0.622 ± 0.050
GJ469A	76.41 ± 0.46	1	187.237102	+8.424238	3902745286187581312	72.266 ± 0.696	201.12	21.31	10.866 ± 0.006	2.781 ± 0.006
AM CVn	1.65 ± 0.3	1	188.727770	+37.628978	1519860699806445184	3.311 ± 0.030	1.86	1.07	14.059 ± 0.003	-0.283 ± 0.009
EX Hya	15.5 ± 0.29	1	193.100317	-29.248754	6185040879503491584	17.572 ± 0.017	2.65	1.08	13.246 ± 0.008	0.416 ± 0.034
GP Com	13.34 ± 0.33	1	196.425059	+18.017867	3938156295111047680	13.731 ± 0.045	1.21	1.04	15.929 ± 0.004	0.021 ± 0.014
V803 Cen	2.88 ± 0.24	1	200.935556	-41.741460	6137049739573759872	3.489 ± 0.060	12.95	1.66	15.731 ± 0.106	0.232 ± 0.475
NSVS 0103	14.92 ± 0.53	6	206.392715	+79.397010	1715299716278321408	16.572 ± 0.018	11.67	1.51	12.363 ± 0.004	2.451 ± 0.012
NSVS 0103-REF68	14.84 ± 0.66	6	206.476952	+79.387440	1715287999607537408	16.576 ± 0.018	4.20	1.17	14.486 ± 0.003	2.741 ± 0.007
CR Boo	2.97 ± 0.34	1	207.229937	+7.959982	3721961488404743040	2.844 ± 0.037	-1.98	0.93	15.467 ± 0.052	0.066 ± 0.208
Proxima Cen	768.7 ± 0.3	1	217.392321	-62.676075	5853498713190525696	768.067 ± 0.050	-1.20	0.97	8.985 ± 0.003	3.805 ± 0.006
G166-037	5.2 ± 0.7	1	218.712738	+25.166043	1255095276181144320	5.155 ± 0.014	1.59	1.06	12.453 ± 0.003	0.911 ± 0.005
HD 128311	60.53 ± 0.15	1	219.003258	+9.745402	1176209886733406592	61.279 ± 0.043	5.14	1.31	7.181 ± 0.003	1.164 ± 0.005
HD 132475	10.18 ± 0.21	1	224.954678	-22.014952	6232043867720079616	10.671 ± 0.025	3.22	1.16	8.391 ± 0.003	0.794 ± 0.005
HD 136118	19.12 ± 0.22	1	229.730587	-1.592288	4415515934099120768	19.812 ± 0.034	8.15	1.43	6.813 ± 0.003	0.690 ± 0.005
GU Boo	3.15 ± 0.56	6	230.478556	+33.935715	1278589709364139520	6.187 ± 0.011	1.39	1.04	13.044 ± 0.003	1.663 ± 0.009
HP Lib	5.07 ± 0.33	1	233.971000	-14.220117	6265476408553544320	3.567 ± 0.031	2.31	1.11	13.603 ± 0.003	-0.153 ± 0.006
HD 140283	17.15 ± 0.14	1	235.757857	-10.934848	6268770373590148224	16.267 ± 0.026	1.31	1.06	7.036 ± 0.003	0.759 ± 0.005
G16-025	3.8 ± 1	1	240.339103	+5.393949	4425854676297423104	3.433 ± 0.014	0.75	1.03	13.146 ± 0.003	0.849 ± 0.005
GJ623A	125 ± 0.3	1	246.046510	+48.350869	1411178510887026048		775.27		9.254 ± 0.003	2.401 ± 0.007
UV Oct	1.71 ± 0.1	1	248.103953	-83.903451	5768557209320424320	1.838 ± 0.012	0.00	1.00	9.536 ± 0.010	0.706 ± 0.043
CM Dra	68.23 ± 0.38	6	248.575581	+57.167574	1431176943768690816	67.288 ± 0.034	9.09	1.42	11.491 ± 0.003	2.924 ± 0.005
CM Dra-REF47	65.1 ± 1.4	6	248.580692	+57.174461	1431176943768691328	67.354 ± 0.021	0.36	1.01	14.849 ± 0.003	0.685 ± 0.005
TRES HER0	5.58 ± 0.53	6	252.586282	+46.650513	1407718450873494784	7.158 ± 0.017	2.42	1.09	14.547 ± 0.003	2.585 ± 0.008
HIP 87062	8.21 ± 0.11	1	266.867655	-8.781545	4165370682239910144	8.718 ± 0.019	-3.96	0.88	10.352 ± 0.003	0.889 ± 0.005
X Sgr	3 ± 0.18	1	266.890075	-27.830835	4057701830728920064	2.806 ± 0.140	5.11	1.22	4.327 ± 0.008	1.098 ± 0.029
HIP 87788	10.83 ± 0.13	1	268.993631	-16.411888	4144902306908889600	10.760 ± 0.016	-7.45	0.70	11.095 ± 0.003	0.915 ± 0.005
Barnard Star	545.4 ± 0.3	1	269.448503	+4.739420	4472832130942575872	546.976 ± 0.040	1.89	1.08	8.194 ± 0.003	2.834 ± 0.005
W Sgr	2.28 ± 0.2	1	271.255132	-29.580110	4050309195613114624	2.365 ± 0.176	35.76	3.95	4.585 ± 0.019	1.108 ± 0.078
DQ Her	2.59 ± 0.21	1	271.876040	+45.859101	2116226254706461568	2.016 ± 0.017	1.50	1.06	14.589 ± 0.011	0.462 ± 0.055
WZ Sgr	0.512 ± 0.0373	5	274.248822	-19.075831	4094784475310672128	0.574 ± 0.028	-1.14	0.94	7.682 ± 0.016	1.779 ± 0.065
Y Sgr	2.13 ± 0.29	1	275.345761	-18.860034	4096107909387492992	1.975 ± 0.058	13.06	1.76	5.475 ± 0.012	1.166 ± 0.050
V603 Aql	4.01 ± 0.14	1	282.227705	+0.584085	4266547566124966912	3.106 ± 0.035	0.31	1.01	11.867 ± 0.013	0.172 ± 0.060
V1223 Sgr	1.96 ± 0.18	1	283.759644	-31.163883	6760253239457454592	1.745 ± 0.024	1.66	1.08	13.029 ± 0.006	0.135 ± 0.026
κ Pav	5.57 ± 0.28	1	284.237527	-67.233423	6434564460631076864	5.245 ± 0.122	37.63	2.29	4.263 ± 0.010	0.915 ± 0.041
FF Aql	2.81 ± 0.18	1	284.561446	+17.360872	4514145288240593408	1.906 ± 0.071	1.51	1.05	5.171 ± 0.005	1.056 ± 0.018
GJ748A	98.4 ± 0.3	1	288.068738	+2.884048	4268226078065241600		1152.54		9.886 ± 0.010	2.624 ± 0.014
RR Lyr	3.77 ± 0.13	1	291.365640	+42.783489	2125982599343482624	3.985 ± 0.026	0.93	1.04	7.619 ± 0.015	0.574 ± 0.062
XZ Cyg	1.67 ± 0.17	1	293.122787	+56.388085	2142052889490819328	1.586 ± 0.015	4.09	1.17	9.914 ± 0.006	0.639 ± 0.031
S Vul	0.322 ± 0.0396	5	297.099176	+27.286481	2027971514401523456	0.205 ± 0.020	1.13	1.03	8.152 ± 0.007	2.231 ± 0.033
GJ1245A	219.9 ± 0.5	1	298.479759	+44.412330	2079074130463898624		1646.33		11.535 ± 0.003	3.701 ± 0.007
GJ1245C	219.9 ± 0.5	1	298.481926	+44.412906	2079073928612821760	214.575 ± 0.048	15.35	1.61	11.908 ± 0.003	3.823 ± 0.005
NGC6853	2.47 ± 0.16	1	299.901564	+22.721214	1827256624493300096	2.570 ± 0.037	5.53	1.16	14.037 ± 0.003	-0.541 ± 0.005
HIP 98492	3.49 ± 0.14	1	300.139629	+9.352701	4299974407538484096	2.660 ± 0.018	-4.13	0.85	11.373 ± 0.003	0.898 ± 0.005
WZ Sge	22.97 ± 0.15	1	301.902433	+17.703984	1809844934461976832	22.104 ± 0.030	1.29	1.04	15.181 ± 0.004	0.170 ± 0.017
GJ791.2A	113.4 ± 0.2	1	307.454338	+9.689504	1752805741531173632		1078.85		11.485 ± 0.003	3.168 ± 0.006

Table 1. continued.

Identifier	parallax (mas)	Ref.	Ra (deg)	Dec (deg)	Source ID	parallax (mas)	GoF	RUWE	G (mag)	$(G_{BP} - G_{RP})$ (mag)
T Vul	1.9 ± 0.23	1	312.867677	+28.250482	1857884212378132096	1.688 ± 0.058	5.28	1.20	5.500 ± 0.010	0.824 ± 0.041
HIP 103269	14.12 ± 0.1	1	313.820146	+42.298456	2065901676227318272	13.960 ± 0.012	-1.26	0.95	10.091 ± 0.003	0.844 ± 0.005
HD 202206	22.98 ± 0.13	1	318.740516	-20.789745	6832155218215202944	21.939 ± 0.028	0.82	1.03	7.922 ± 0.003	0.848 ± 0.005
GJ831A	125.3 ± 0.3	1	322.832981	-9.790965	6894054664842632448		1186.79		10.471 ± 0.003	3.083 ± 0.008
HIP 106924	14.47 ± 0.1	1	324.813858	+60.284865	2203746967971153024	15.019 ± 0.012	-5.10	0.79	10.155 ± 0.003	0.871 ± 0.005
SS Cyg	8.3 ± 0.41	1	325.679037	+43.586222	1972957892448494592	8.854 ± 0.030	33.77	2.33	11.671 ± 0.014	1.177 ± 0.078
HIP 108200	12.4 ± 0.09	1	328.821293	+32.645318	1946297900868982016	12.373 ± 0.014	3.43	1.09	10.783 ± 0.003	0.932 ± 0.005
RU Peg	3.55 ± 0.26	1	333.510604	+12.703148	2727974767550030080	3.662 ± 0.021	5.72	1.29	12.334 ± 0.012	0.964 ± 0.058
PN DeHt5	2.9 ± 0.15	1	334.890158	+70.934134	2229624931896924160	2.982 ± 0.036	5.46	1.22	15.462 ± 0.003	-0.304 ± 0.006
HD 213307	3.65 ± 0.15	1	337.288645	+58.404113	2200153214212849024	3.454 ± 0.051	9.58	1.42	6.300 ± 0.003	-0.025 ± 0.005
δ Cep	3.66 ± 0.15	1	337.292885	+58.415208	2200153454733285248	3.555 ± 0.147	31.03	2.71	3.851 ± 0.014	0.971 ± 0.057
NGC7293	4.64 ± 0.27	1	337.410790	-20.837167	6628874205642084224	5.012 ± 0.044	-1.02	0.95	13.459 ± 0.003	-0.588 ± 0.006
RZ Cep	2.12 ± 0.16	1	339.805873	+64.859351	2211629018927324288	2.401 ± 0.012	-0.29	0.99	9.294 ± 0.009	0.740 ± 0.039
GJ 876	214.6 ± 0.2	1	343.324111	-14.266689	2603090003484152064	214.038 ± 0.036	6.49	1.34	8.875 ± 0.003	2.809 ± 0.005
γ Cep	74.27 ± 0.12	1	354.835781	+77.633125	2281778105594488192	72.517 ± 0.147	37.24	3.21	2.943 ± 0.003	1.257 ± 0.022

Notes. Column 1. Identifier. Column 2. Trigonometric parallax with error. Column 3. References for the parallax. 1=Benedict et al. (2017), 2=Bond et al. (2018), 3=Groenewegen (2018), 4=Riess et al. (2014), 5=Riess et al. (2018a), and 6=van Belle et al. (2020), Column 4,5. Ra and Declination from GEDR3. Stars not in GEDR3 have coordinates listed between parentheses. Column 6. source identifier from GEDR3. Column 7. parallax with error from GEDR3. Column 8,9. Goodness-of-fit and Renormalised Unit Weight Error. Column 10,11. G magnitude and $(G_{BP} - G_{RP})$ colour.